



RESEARCH ARTICLE

10.1029/2019MS001732

Key Points:

- A spectral cumulus parameterization was implemented in icosahedral nonhydrostatic atmospheric model (ICON-A)
- The parameterization improved tropical variability simulated in the ICON-A, especially the Madden-Julian oscillation
- Entrainment parameterization, spectral representation, and convective closure contribute to better simulation of Madden-Julian oscillation

Correspondence to:

Y. Baba,
babay@jamstec.go.jp

Citation:

Baba, Y., & Giorgetta, M. A. (2020). Tropical variability simulated in ICON-A with a spectral cumulus parameterization. *Journal of Advances in Modeling Earth Systems*, 12, e2019MS001732. <https://doi.org/10.1029/2019MS001732>

Received 5 MAY 2019

Accepted 25 NOV 2019

Accepted article online 28 DEC 2019

Tropical Variability Simulated in ICON-A With a Spectral Cumulus Parameterization

Yuya Baba¹ and Marco A. Giorgetta²

¹Application Laboratory, Japan Agency for Marine-Earth Science and Technology, Yokohama, Japan, ²Max Planck Institute for Meteorology, Hamburg, Germany

Abstract We implemented a spectral cumulus parameterization based on a cloud-resolving model (SC scheme) in the icosahedral nonhydrostatic atmospheric model (ICON-A). We compared the resulting simulated climatology and tropical variability with results from the standard version of ICON-A using a variant of the Tiedtke-Nordeng scheme (TK scheme) using observational and reanalysis data. The climatological errors of the SC scheme were similar to those of the TK scheme, but several biases, such as properties of meridional winds and precipitation pattern in the western Pacific, were much improved. For tropical variability, we found that the SC scheme improved the interannual response of the precipitation in the western Pacific and was able to simulate Madden-Julian oscillation (MJO) features much better than the TK scheme. We investigated the reason for the better simulation of the MJO using composite analysis and column process analysis for moisture. Our results suggest that the entrainment parameterization of the SC scheme is necessary to reproduce the MJO; however, spectral representation and improved convective closure are also found to contribute for better MJO simulation. These parameterizations improved moisture supply from low-level clouds and cloud mass flux which were needed to sustain the MJO.

Plain Language Summary Atmospheric general circulation models, as used in climate research, still use horizontal resolutions of typically 100 km to allow integrations over many years or decades. Such models therefore cannot resolve the much smaller scales of convective clouds, and consequently, their important effects on the general circulation and climate need to be parameterized, that is, represented in a simplified way depending on the resolved scales of the atmospheric model. Due to the complications of the dynamics and processes of convective clouds, a large uncertainty exists in parameterizing convection. In this study, we implement and evaluate a recently developed convection scheme that considers the unresolved cloud structure more accurately in the icosahedral nonhydrostatic atmospheric model (ICON-A). The evaluation results showed particular improvement for intraseasonal variability dominated by organized convection consisting of various different clouds (i.e., Madden-Julian oscillation). We also provide analysis to explain this improvement and focus on the contributions of the scheme for simulating the organized convection.

1. Introduction

Cumulus parameterizations (also referred to as convection schemes) are one of the most important physical parameterizations that influence climates simulated by general circulation models (GCMs). In particular, it is known that several features and phenomena of tropical climate system are affected by convection schemes, such as the Intertropical Convergence Zone (ITCZ, e.g., Bellucci et al., 2010; Wu et al., 2003) and the El Niño–Southern Oscillation (ENSO, e.g., Neale et al., 2008; Watanabe et al., 2011). Convectively coupled equatorial waves (CCEWs) and the Madden-Julian oscillation (MJO, Madden & Julian, 1971; Zhang, 2005) in the tropics are responsible for the atmospheric variability represented by various convective clouds. They play important roles in the global atmospheric circulation. However, the reproducibility of CCEWs is strongly dependent on the convection schemes used in GCMs, and the parameterizations are generally known to be poor in simulating the MJO (Hung et al., 2013; Lin et al., 2008). There are several possible reasons for this drawback, including that convection schemes cannot adequately represent various structures of convective clouds associated with the MJO; that is, the representation of unresolved convective cloud structures is inaccurate. Several recent parameterizations that more accurately considered unresolved convective structures succeeded in simulating reasonable CCEWs and MJO behaviors (e.g., Baba, 2019; Chikira & Sugiyama,

©2019. The Authors.

This is an open access article under the terms of the Creative Commons Attribution License, which permits use, distribution and reproduction in any medium, provided the original work is properly cited.

2013; Zhang & Song, 2009). However, their validities in different GCMs (having different nonconvective parameterizations) unfortunately remain uncertain.

The recently developed convection scheme of Baba (2019) has been implemented in a GCM, known as the icosahedral nonhydrostatic atmospheric model in a configuration for climate simulation: ICON-A (Giorgetta et al., 2018). ICON-A combines the nonhydrostatic dynamical core of Zängl et al. (2015) with a physics package adopted from ECHAM6 GCM (Giorgetta et al., 2013; Stevens et al., 2013). To evaluate the model, Crueger et al. (2018) conducted diagnoses of the simulated atmospheric circulation using ICON-A in an atmospheric model intercomparison project (AMIP) experiment, revealing that ICON-A showed comparable performance with ECHAM6. However, there were differences in the results; that is, the simulated climatology of ICON-A was better than ECHAM6 in the extratropics but worse in the tropics. Meanwhile, although tropical variability was slightly improved, MJO-related variability was still lacking. These trends may stem from tuning of model parameters for ICON-A but still remained as an open question (Crueger et al., 2018). Since tropical climatology and variability are sensitive to uncertainties existing in the convection scheme, an improvement of the scheme will contribute to the further improvement of tropical climatology and variability of the model.

Recently, Baba (2019) developed a spectral cumulus parameterization based on cloud-resolving model simulations and statistical analysis of the structure of convective clouds, aimed at simulating unresolved convective cloud structures more precisely than in existing schemes. The scheme of Baba (2019) is different from the single-plume bulk-mass-flux convection scheme (e.g., Tiedtke, 1989) employed in ICON-A, as it employs a spectral representation for convective clouds that can represent coexisting convective clouds of different types in a single grid column. The scheme was found to be able to simulate reasonable CCEWs and MJO behaviors in the AMIP experiment. This may have been due to the fact that the unresolved clouds were more accurately considered using the spectral representation and improved in-cloud parameterization. The features of spectral cumulus parameterization help improve the simulation results using ICON-A in the tropics. Further, the scheme may elucidate why the original convection scheme of ICON-A does not simulate tropical variability as well.

In this study, we evaluate the spectral cumulus parameterization (Baba, 2019) in ICON-A, comparing the results with those obtained with the original convection scheme of ICON-A (Nordeng, 1994; Tiedtke, 1989), using observational and reanalysis data. The focus will be especially on the analysis of the improvements in simulating the climatology and variability in the tropical circulation in the AMIP experiment. In section 2, we describe details of the convection schemes and the differences between the two convection schemes. Section 3 provides details of the atmospheric GCM (AGCM) used in this study and the experimental setup. In section 4, climatological errors, mean state, and tropical variability are discussed. Results from further analysis on intraseasonal variability are presented in section 5, related to earlier studies, which showed that some bulk convection schemes were able to simulate the tropical variability and MJO (e.g., Hirono et al., 2013; Hung et al., 2013; Kim et al., 2009). Therefore, section 5 makes use of additional sensitivity experiments to discuss separately impact of spectral representation and in-cloud parameterizations. Then, using the composite analysis on the convective fields and moisture variation, we investigate the impact of convection schemes on the convective organization. Section 6 presents summary and conclusion.

2. Convection Schemes

2.1. Tiedtke Scheme

The original configuration of ICON-A employs the Tiedtke scheme (Tiedtke, 1989), which includes modifications by Nordeng (1994) and has been ported from ECHAM6 (Tiedtke-Nordeng scheme, TK scheme hereafter). This scheme is essentially a categorical bulk mass flux scheme; that is, depending on the criteria, each convective column is identified as a deep-, shallow-, or middle-level convective column, and its properties are then calculated (Möbis & Stevens, 2012). The entrainment and detrainment rates for deep convection in this scheme consist of organized and turbulent parts. The organized entrainment rate for deep convection is given by

$$\epsilon_u^{\text{org}} = \frac{B_u}{2 \left(w_b^2 + \int_{z_b}^{z_t} B_u dz \right)} + \frac{1}{\bar{\rho}} \frac{\partial \bar{\rho}}{\partial z}, \quad (1)$$

where B_u is the in-cloud buoyancy, $w_b = 1$ m/s the cloud base updraft velocity, z_b the cloud base height, z_t the cloud top height, z the vertical coordinate, and $\bar{\rho}$ the environmental density, where the overbar denotes environmental values. The organized detrainment rate for deep convection is defined using the fractional cloudy area σ by

$$\delta_u^{\text{org}} = \frac{1}{\sigma} \frac{\partial \sigma}{\partial z}, \quad (2)$$

where σ is given as a function of the vertical coordinate. Note that, for shallow- and middle-level convection, the organized entrainment and detrainment rates are set to 0. Turbulent quantities for each cloud type are set to be constant but switched on or off depending on the pressure levels (Möbis & Stevens, 2012). In the implementation of ECHAM physics in ICON-A, the parameters of turbulent quantities were modified. The turbulent entrainment (detrainment) rates are set to $2 \times 10^{-4} \text{ m}^{-1}$ for deep- and middle-level convection, $3 \times 10^{-3} \text{ m}^{-1}$ for shallow convection, and $4 \times 10^{-4} \text{ m}^{-1}$ for downdraft (Giorgetta et al., 2018).

To determine the strength of cloud mass flux, a closure based on convective available potential energy (CAPE) is adopted. The time derivative of CAPE due to atmospheric stabilization by convection is given by (Giorgetta et al., 2013)

$$\frac{\partial \text{CAPE}}{\partial t} \approx - \int_{z_b}^{z_t} \frac{g}{\bar{T}_v} \frac{\partial \bar{T}_v}{\partial t} dz = - \int_{z_b}^{z_t} \left(\frac{1 + \epsilon \bar{q}}{c_p \bar{T}} \frac{\partial \bar{s}}{\partial z} + \epsilon \frac{\partial \bar{q}}{\partial z} \right) \frac{g}{\bar{\rho}} M dz, \quad (3)$$

where t is time, g the gravitational acceleration, T_v the virtual temperature, c_p the specific heat at constant pressure, T the temperature, s the dry static energy, q the specific humidity, $\epsilon = R_v/R_d - 1$ (R_v : gas constant for vapor, R_d : gas constant for air), and M the cloud mass flux. Assuming the CAPE is relaxed by convective stabilization with a time scale τ , the time derivative can be expressed as

$$\frac{\partial \text{CAPE}}{\partial t} = \frac{\text{CAPE}}{\tau}, \quad \text{CAPE} = \int_{z_b}^{z_t} g \left(\frac{T_{v,u} - \bar{T}_v}{\bar{T}_v} - l_u \right) dz, \quad (4)$$

where $T_{v,u}$ is the virtual temperature in convective updraft and l_u the updraft cloud condensate. Using equations (3) and (4) and assuming $M = M^* \cdot M_b/M_b^*$, the final cloud base mass flux is given by

$$M_b = M_b^* \frac{\text{CAPE}}{\tau} \frac{1}{\int_{z_b}^{z_t} \left(\frac{1 + \epsilon \bar{q}}{c_p \bar{T}} \frac{\partial \bar{s}}{\partial z} + \epsilon \frac{\partial \bar{q}}{\partial z} \right) \frac{g}{\bar{\rho}} M^* dz}, \quad (5)$$

where M_b is the (updated) cloud base mass flux, the M_b^* its provisional value, and M^* the provisional cloud mass flux. The adjustment time scale τ was specified as 1 hr for ICON-A.

A different closure is applied to shallow convection (Möbis & Stevens, 2012), which is given as

$$M_b = \frac{\int_{z_s}^{z_b} \frac{\partial \bar{q}}{\partial t} \bar{\rho} dz}{[q_u + l_u - 0.3 q_d - 0.7 \bar{q}]_{\text{base}}}, \quad (6)$$

where z_s is the surface height, $\partial \bar{q}/\partial t$ the moisture tendency before convection, q_u the updraft specific humidity, and q_d the downdraft specific humidity. The subscript *base* indicates the value at the cloud base height. This closure is based on the assumption that the moisture flux at the cloud base height is balanced with the flux induced by subcloud layer (Tiedtke, 1989). After updating the cloud base mass flux, the provisional cloud base mass flux is changed by the updated value, and all the quantities relating to cloud mass flux are rescaled by multiplying all the terms in the budget equations by M_b/M_b^* .

A potential problem of this TK scheme is that the convective structure to be computed at each time step is restricted by the assumed cloud type, which is identified by the employed criteria. For instance, if the convective column is identified as shallow convection, even though there are some probabilities that deep convection can occur, the parameterizations and parameters for shallow convection are nonetheless chosen. As the result of this switching, the structure of deep convection will be missed in the grid column at this time step.

2.2. Spectral Cumulus Parameterization

Spectral cumulus parameterization based on a cloud-resolving model (Baba, 2019) was implemented in ICON-A (SC scheme hereafter). The SC scheme consists of the modified in-cloud parameterization of Gregory (2001) that relates entrainment rate, in-cloud buoyancy, and detrainment rate to each other. The in-cloud equations used in this scheme are given as

$$\epsilon_u = \frac{C_1 B_u - C_2 \delta_u w_u^2}{w_u^2}, \quad (7)$$

$$\frac{1}{2} \frac{\partial w_u^2}{\partial z} = a B_u - b \delta_u w_u^2 - \epsilon_u w_u^2, \quad (8)$$

where ϵ_u is the updraft entrainment rate, δ_u the updraft detrainment rate computed by the model of Derbyshire et al. (2011), w_u the cloud mean updraft velocity, and B_u the in-cloud buoyancy. Here, equation (8) is identical to that proposed in Simpson and Wiggert (1969) and employed in Gregory (2001), except for the values of parameters. C_1 , C_2 , a , and b are model parameters determined based on statistical analysis of the convective cloud structures ($C_1 = C_2 \approx 0.2$, $a = C_1 + 0.5$, and $b = C_2 + 0.75$). The above in-cloud parameterization and model parameters were led by measuring the values of in-cloud quantities and assuming the relationship between ϵ_u , B_u , w_u , and δ_u from model output of long-term cloud-resolving model simulation. Note that the above entrainment and detrainment rates are used for all cloud types. To spectrally represent different convective clouds, 14 cloud types are defined as in Chikira and Sugiyama (2010) and the above equations are used to determine updraft properties of each cloud type. Each cloud type was characterized by spectrally distributed cloud base updraft velocities, ranging from 0.1 to 1.4 m/s. The updraft mean properties are obtained by averaging over all convective cloud types using weighting factors and the cloud mass fluxes. In addition to the above entrainment and detrainment, their turbulent components are introduced to tune the cloud cover based on European Centre for Medium-Range Weather Forecast (ECMWF, 2008, 2014) with the set of physical parameterization of ICON-A and resulting atmospheric energy budget (Appendix A).

In the implementation of the SC scheme in ICON-A, different closures are applied to cloud types classified as deep and shallow convection. Diagnostic density-weighted CAPE closure (Bechtold et al., 2014) was applied for all the cloud types in the original SC scheme although the closure was originally designed only for deep convection. In the modified scheme, this closure is applied only for deep convection, and another closure is applied to shallow convection. To apply different closures for different cloud types, the updraft mean convective properties for deep convection are computed from the summation of quantities of all cloud types j with a convective depth thicker than 180 hPa (which is the modified value of 200 hPa employed in Bechtold et al., 2014) as

$$M_{u,dep} = \sum_j M_u^j, \quad \phi_{u,dep} = \frac{\sum_j M_u^j \phi_u^j}{M_{u,dep}}, \quad (9)$$

where $M_{u,dep}$ is the bulk cloud mass flux of deep convection and $\phi_{u,dep}$ the corresponding in-cloud quantity. The values corresponding to shallow convection are denoted as $M_{u,sha}$ and $\phi_{u,sha}$ hereafter and are computed in the same manner as in equation (9), but the updraft quantities for shallow convection are identified by the convective depth which is thinner than 180 hPa.

In the original SC scheme, the convective closure was applied to the cloud mass fluxes after first calculating the convective updraft properties. In the modified scheme, however, the closure for deep convection is applied after calculating both the updraft and downdraft properties. The formulation of the closure (Bechtold et al., 2014) is given by

$$M_{b,dep} = M_{b,dep}^* \frac{PCAPE}{\tau} \frac{1}{\int_{z_b}^{z_t} \frac{g}{\bar{T}_v} \left(\frac{\partial \bar{T}_v}{\partial z} + \frac{g}{c_p} \right) M_{dep}^* dz}, \quad M_{b,dep} > 0, \quad (10)$$

$$PCAPE = \int_{z_b}^{z_t} g \frac{T_{v,u,dep} - \bar{T}_v}{\bar{T}_v} \bar{\rho} dz, \quad (11)$$

where $PCAPE$ is the density-weighted CAPE and $\tau = 1$ hr. Here, density-weighted CAPE is used instead of CAPE to relate CAPE change to cloud base mass flux directly, considering layer thickness in the atmospheric

instability. Note that $M_{b,dep}^*$ and the in-cloud values used above are obtained from the mean updraft properties of deep convection. M_{dep}^* is the provisional cloud mass flux consisting of updraft and downdraft mass fluxes as $M_{dep}^* = M_{u,dep}^* + M_{d}^*$.

The shallow convective closure (Bechtold et al., 2014) is given as

$$M_{b,sha}(h_u - \bar{h})_{base} = \int_{z_s}^{z_b} \frac{\partial \bar{h}}{\partial t} \Big|_{bl} \bar{\rho} dz, \quad M_{b,sha} > 0, \quad (12)$$

where $M_{b,sha}$ is the cloud base mass flux for shallow convection, h_u is the updraft moist static energy (MSE), and \bar{h} the environmental MSE. The subscript *bl* indicates the tendency from the boundary layer process except for the convection. The subscript *base* means the value at the cloud base height. Note that the value of $(h_u)_{base}$ is common for deep and shallow convection. To consider downdraft effect on this closure, \bar{h} is replaced by $\beta h_d + (1 - \beta)\bar{h}$, where h_d is the downdraft MSE and $\beta = (M_d^*/M_{u,sha}^*)_{base}$ (ECMWF, 2014). The resulting final updated cloud base mass flux is given as $M_b = M_{b,dep} + M_{b,sha}$, and thus, the rescaling for the mean bulk updraft and downdraft properties can be done using the rescaling factor of $M_b/M_b^* = (M_{b,dep} + M_{b,sha})/M_b^*$.

The main differences between the SC and TK schemes are the representation of different convective cloud types, organized entrainment and detrainment, and convective closure. Since the SC scheme allows coexistence of different cloud types, a flexible representation for coexisting convective clouds is possible. Therefore, simulated convective cloud structures are expected to be different from those simulated by the TK scheme. The organized entrainment and detrainment rates of the SC scheme are based on cloud-resolving model simulations so that the identical formulation can be employed for different cloud types. Hence, uncertainties deriving from empirical formulations for identifying each cloud type can be reduced and the different cloud types are continuously represented by the identical formulation. The difference in the convective closure can be regarded as a difference in conversion of CAPE change to mass flux change. The density-weighted CAPE closure can more directly relate the time derivative of CAPE to mass flux change and can take the atmospheric instability into account more correctly considering layer thickness (Bechtold et al., 2014). Thus, the scheme is expected to avoid over or underestimation of the mass flux change by the change of CAPE.

3. Model and Experimental Setup

ICON-A used as the AGCM for the present study consists of a nonhydrostatic dynamical core employing the icosahedral C-grid system (Wan et al., 2013; Zängl et al., 2015). The model employs the physics packages of ECHAM6 for the atmosphere and the Jena Scheme for Biosphere Atmosphere Coupling in Hamburg for the land (Giorgetta et al., 2013). The mean horizontal resolution of ICON-A for our AMIP experiment is approximately 160 km and we use 47 vertical layers resolving the atmosphere up to 80 km. These choices for the horizontal and vertical resolution are identical to those used in Giorgetta et al. (2018). Note that the ICON-A version used here has been updated from Giorgetta et al. (2018) and includes bug fixes in the vertical diffusion scheme; thus, the results in this study are slightly different from those presented in Giorgetta et al. (2018) and Crueger et al. (2018).

The AMIP experiments were performed following the AMIP II protocol (Taylor et al., 2000). The transient forcing of the AMIP experiment follows the recommendations of CMIP6 (Eyring et al., 2016). The monthly mean sea surface temperature (SST), sea ice concentration (PCMDI, 2017), solar irradiance, ozone concentration, and greenhouse gas concentrations (Meinshausen et al., 2017) are prescribed and used for forcing of the experiments. Radiative properties of anthropogenic aerosols are calculated by the second version of the Max Planck Institute Aerosol Climatology (MACv2-SP) parameterization (Fiedler et al., 2017; Stevens et al., 2017). The atmosphere of the experiments is initialized by ECMWF reanalysis data (ERA-interim, Dee et al., 2011). The time integration was performed for 10 years from 1 January 1979 to 31 December 1988, as in Giorgetta et al. (2018). This relatively short integration term compared to the ordinary climate runs was chosen based on the preceding studies that validated reproducibility of the MJO (e.g., Baba, 2019; Cai et al., 2013; Chikira & Sugiyama, 2013; Zhang & Song, 2009). Two AMIP experiments were performed using TK and SC schemes, and these cases are, respectively, referred to as AMIP-TK and AMIP-SC. Except for the difference in the convection scheme, both experiments use the same tuning parameters for all other physical parameterizations as in Giorgetta et al. (2018). In the following analysis, daily mean variables are analyzed, and the model variables defined on the icosahedral grid are interpolated onto a 2° longitude-latitude grid because

Table 1
Observational and Reanalysis Data Used for the Model Evaluation

Quantity	Name	Reference
Zonal and meridional winds monthly	ERA-interim	Dee et al. (2011)
Air temperature monthly	ERA-interim	Dee et al. (2011)
Specific humidity monthly	ERA-interim	Dee et al. (2011)
Total precipitation monthly	GPCP ver.2-2	Adler et al. (2003)
Total precipitation daily	GPCP ver.1-2	Huffman et al. (2001)
Precipitable water monthly	ERA-interim	Dee et al. (2011)
Sea level pressure monthly	ICOADS	Woodruff et al. (2011)
TOA radiative flux monthly	CERES-EBAF	Loeb et al. (2009)
TOA radiative flux daily	AVHRR	Liebmann and Smith (1996)
Cloud cover monthly	CALIPSO-GOCCP	Chepfer et al. (2010)
Surface wind stress monthly	ERA-interim	Dee et al. (2011)

Note. TOA refers to top of atmosphere.

this study focuses on spatially large and long time scales, that is, climatology and at least intraseasonal time scale.

4. Climatology and Variability

4.1. Standardized Error Analysis for Climatology

As described in section 1, convection schemes have critical impacts on the simulated climate by AGCMs. Thus, it is worth evaluating the climatological errors simulated by the AGCMs with different convection schemes. The errors were validated against observational and reanalysis data. The same standardized error analysis (Reichler & Kim, 2008) done in the evaluation of ECHAM6 (Stevens et al., 2013) and ICON-A (Crueger et al., 2018) was also performed for the present results. The observational and reanalysis data used for the error analysis and later evaluation are listed in Table 1. For simplicity, these data are referred as observation hereafter. The results of AMIP-TK were used as the reference experiment in the standardized error analysis.

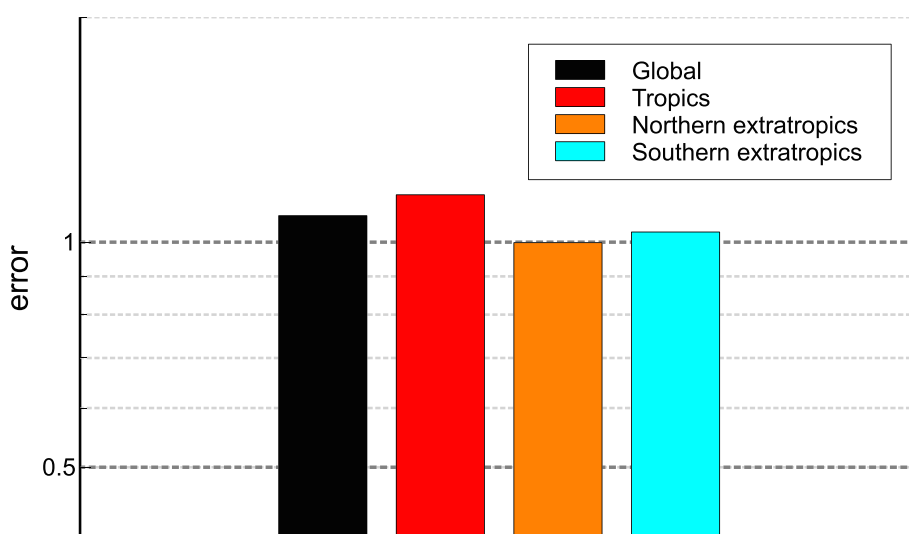


Figure 1. Total standardized errors of the AMIP-SC experiment in global and different latitudinal regions using errors from the AMIP-TK experiment as reference values. Tropics, northern extratropics, and southern extratropics are regionally averaged values and the regions are defined by the ranges of latitudes between 30°S to 30°N, 30–90°N, and 90–30°S, respectively. A value of 1 means that the systematic errors of AMIP-SC with respect to the observations are the same as for AMIP-TK.

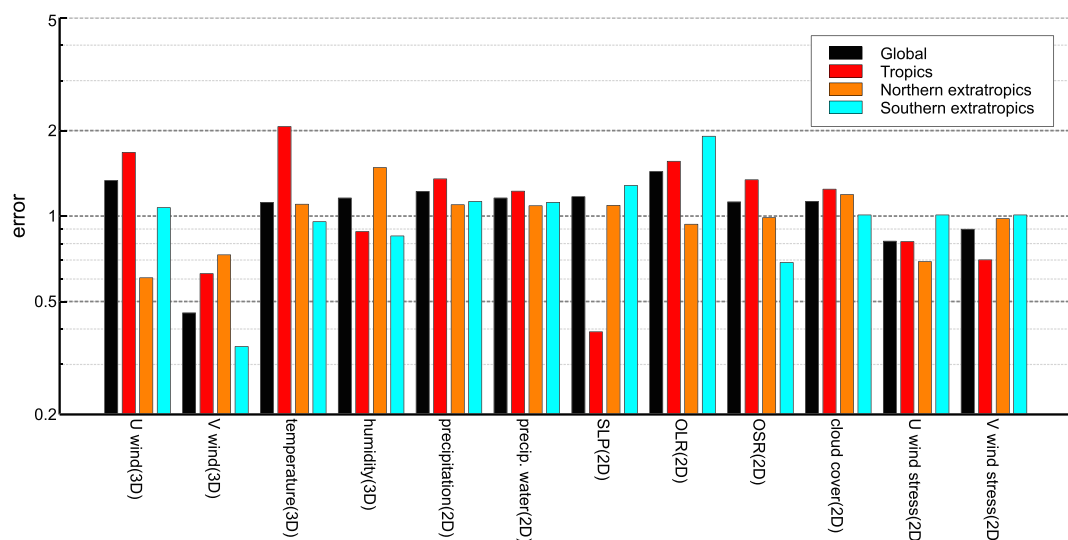


Figure 2. Same as Figure 1 but for each variable. U, V, OLR, and OSR indicate zonal wind, meridional wind, outgoing longwave radiation, and outgoing shortwave radiation, respectively. Two-dimensional and 3-D, respectively, indicate that the values are two-dimensional values or three-dimensional values (with the zonal mean at 1,000- to 100-mb levels, with 100-mb interval).

The standardized errors that can be regarded as climatological errors of AMIP-SC with respect to AMIP-TK are shown in Figure 1. It is apparent that AMIP-SC showed slightly worse results in the climatology of tropics, but the global errors were comparable. This is because error in the extratropics is slightly improved. The errors in the northern and southern extratropics are different, and the improvement is seen especially in the northern part (the error is 0.975). The comparison of the errors for each variable is shown in Figure 2. In the tropics, improvements in the meridional wind, humidity, and sea level pressure were significant, but errors were larger in the zonal wind, temperature, and radiative fluxes, which include outgoing longwave and shortwave radiative fluxes (OLR and OSR). In the northern extratropics, most errors are comparable, but the zonal and meridional wind error decreases are remarkable. In the southern extratropics, some errors (e.g., sea level pressure and OLR) increased, but other errors (e.g., meridional wind, humidity, and OSR) showed remarkable improvements. From our results, the meridional wind error was drastically improved throughout the different latitudes and the errors of other variables were eventually found to be comparable. The improvement in the meridional wind might be related to the change in the Hadley circulation because it can be affected by tropical convective activity and the activity is altered by the convection schemes.

4.2. Mean State

The mean state of the simulated atmospheric circulation was validated by comparing the results with the observation. Annual mean precipitation patterns are compared in Figure 3, indicating that AMIP-SC improves precipitation pattern in the western Pacific compared with AMIP-TK. In this region, AMIP-TK simulates a widely separated ITCZ and South Pacific Convergence Zone (SPCZ), but this bias is reduced with the SC scheme. Further, the northward shifted SPCZ observed in AMIP-TK is also improved in AMIP-SC as the SPCZ is shifted southward. In the Indian Ocean, AMIP-SC mitigates the unrealistic double convergence zone, which appears with the TK scheme, but AMIP-SC does not have enough precipitation compared to Global Precipitation Climatology Project (GPCP). As for the amount of precipitation, AMIP-SC seems to simulate too much precipitation over the tropical land with respect to the AMIP-TK and observation.

The annual mean total cloud cover maps are compared in Figure 4. In both cases, AMIP-TK and AMIP-SC commonly simulated too little cloud cover in the subtropical regions. AMIP-SC simulated less cloud cover over the region, but the trend was common for both cases. Thus, this may be attributed to other physical parameterizations than the convection scheme. Another common remarkable bias is too little cloud cover over the Southern Ocean. Simulating the correct amount of cloud cover over the region is known to be difficult (Bodas-Salcedo et al., 2014), and it remains unclear as to what extent this bias can be mitigated through convection scheme modification.

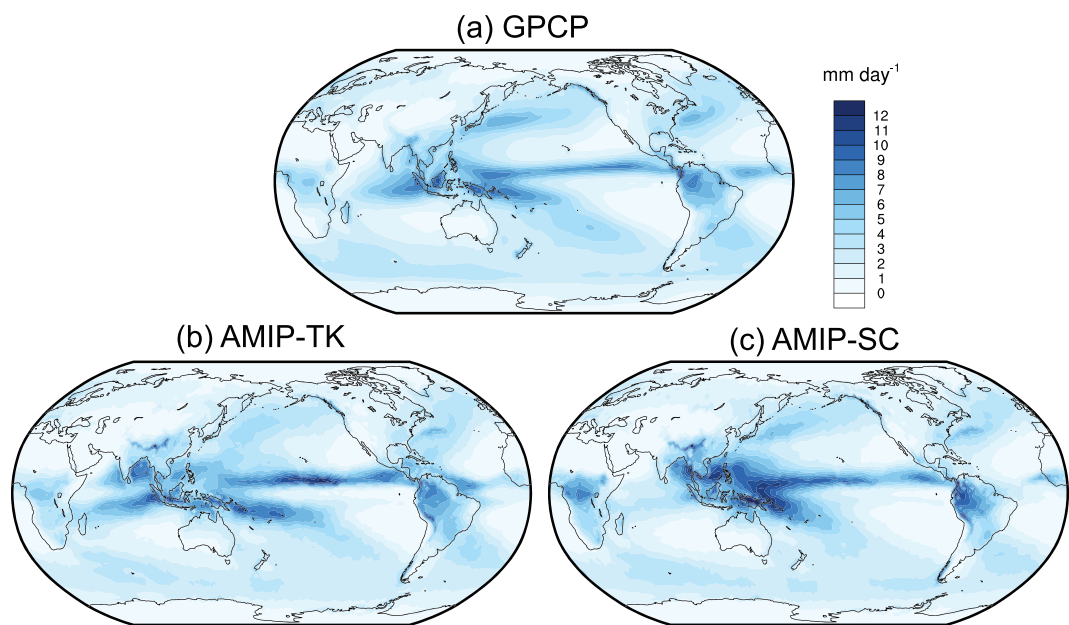


Figure 3. (a–c) Comparison of annual mean precipitation. GPCP data used as the reference were averaged over 10 years from 1979.

Biases of OLR and OSR fluxes are compared in Figure 5a. In AMIP-TK, characteristic common biases are observed for the OLR and OSR over the Maritime Continent as the OLR and OSR showed positive and negative biases, respectively. This means that AMIP-TK simulated less clouds over the region, which is consistent with less precipitation over the western Pacific. On the other hand, the radiative flux biases of AMIP-SC appeared slightly positive over the ocean for OLR and were positive over land in the tropics for OSR. These biases are considered to be derived from the lower cloud cover over the ocean and the strong convection over land in the tropics. The resulting top-of-atmosphere (TOA) net radiative fluxes are compared in Figure 5b. The net radiative flux from the observation shows slightly positive but less than 1 W/m^2 . The net budget simulated by AMIP-SC about -1 W/m^2 , which is more closer to the observation than AMIP-TK. The bias

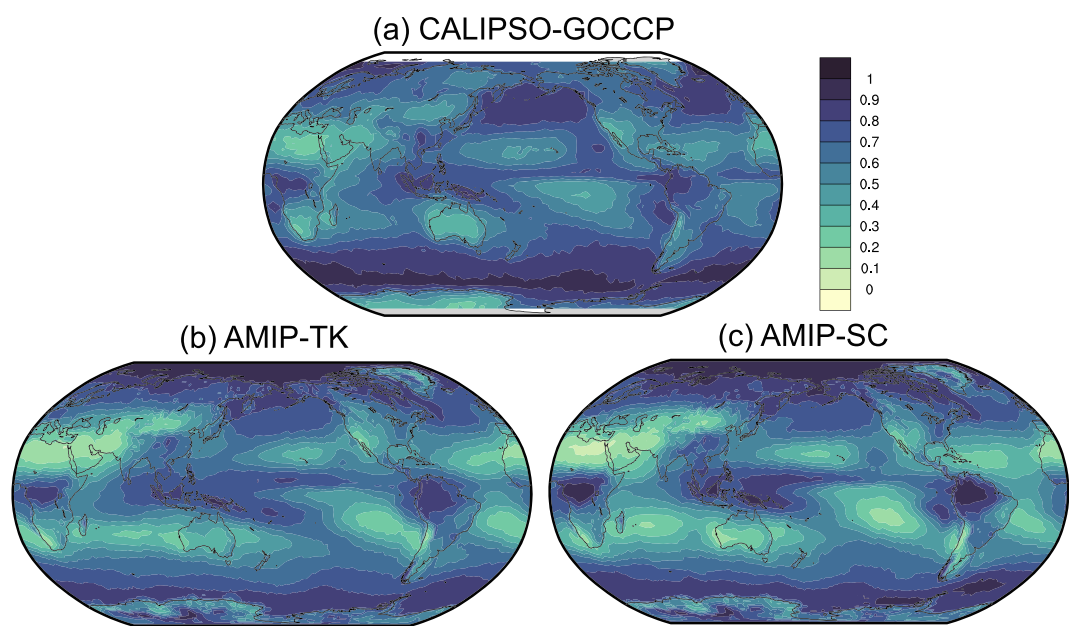


Figure 4. (a–c) Comparison of annual mean total cloud cover. CALIPSO-GOCCP data used as the reference were averaged over 10 years from 2007.

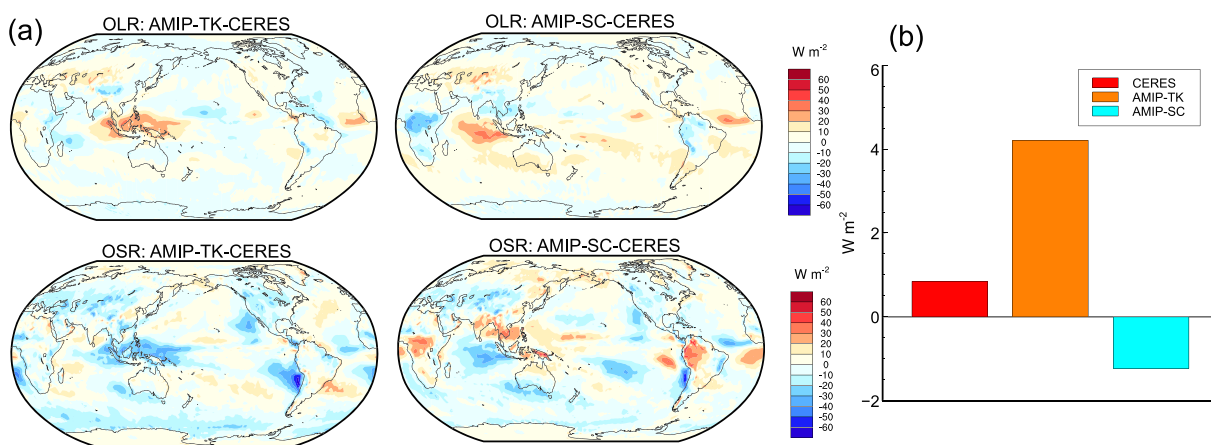


Figure 5. Comparison of (a) biases of annual mean outgoing longwave radiation (OLR) and outgoing shortwave radiation (OSR) and (b) comparison of global mean TOA net radiative flux. CERES-EBAF data used as the reference were averaged over 10 years from 2001.

of AMIP-TK is larger than the +0.5 W/m² reported by Crueger et al. (2018). This was because the ICON-A code used here had not been retuned after including bug fixes which impact the radiation balance at TOA. Obviously, the net radiative flux at TOA could be tuned better for both cases by aiming at a small positive value following the lines of Giorgetta et al. (2018).

Summarizing the mean state biases using different convection schemes, we conclude that the SC scheme is able to improve cloud properties and precipitation in the western Pacific, but it tends to simulate

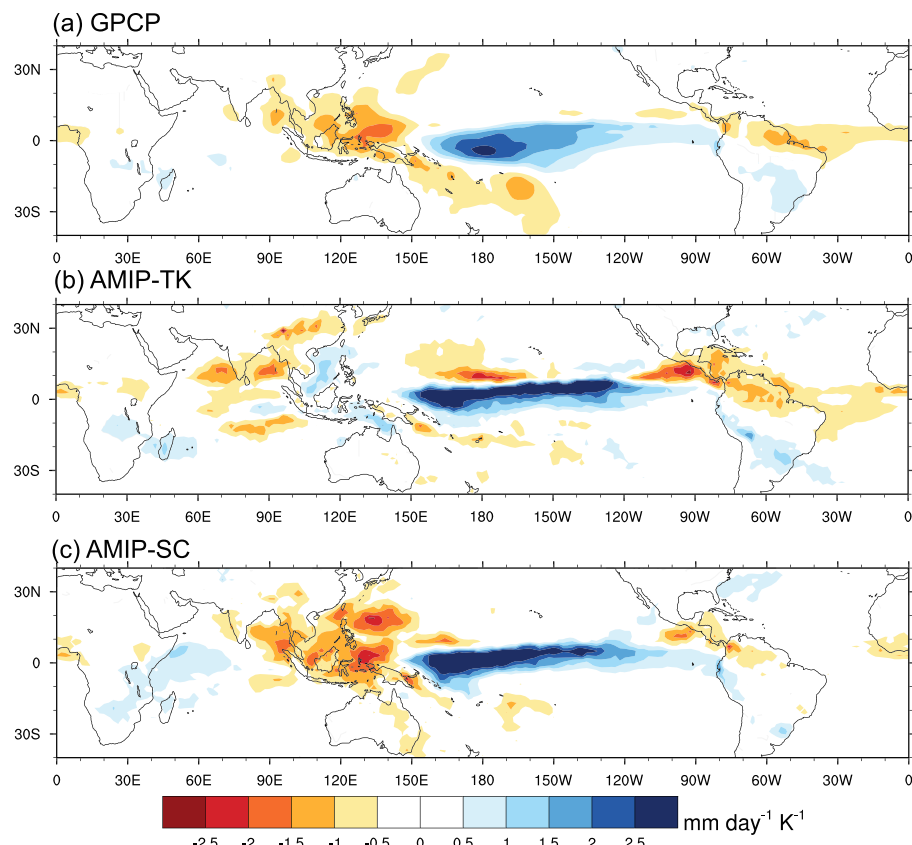


Figure 6. (a–c) Regression of tropical monthly precipitation anomalies onto the Niño 3.4 index. Monthly GPCP data (1979–1988) were used as the reference.

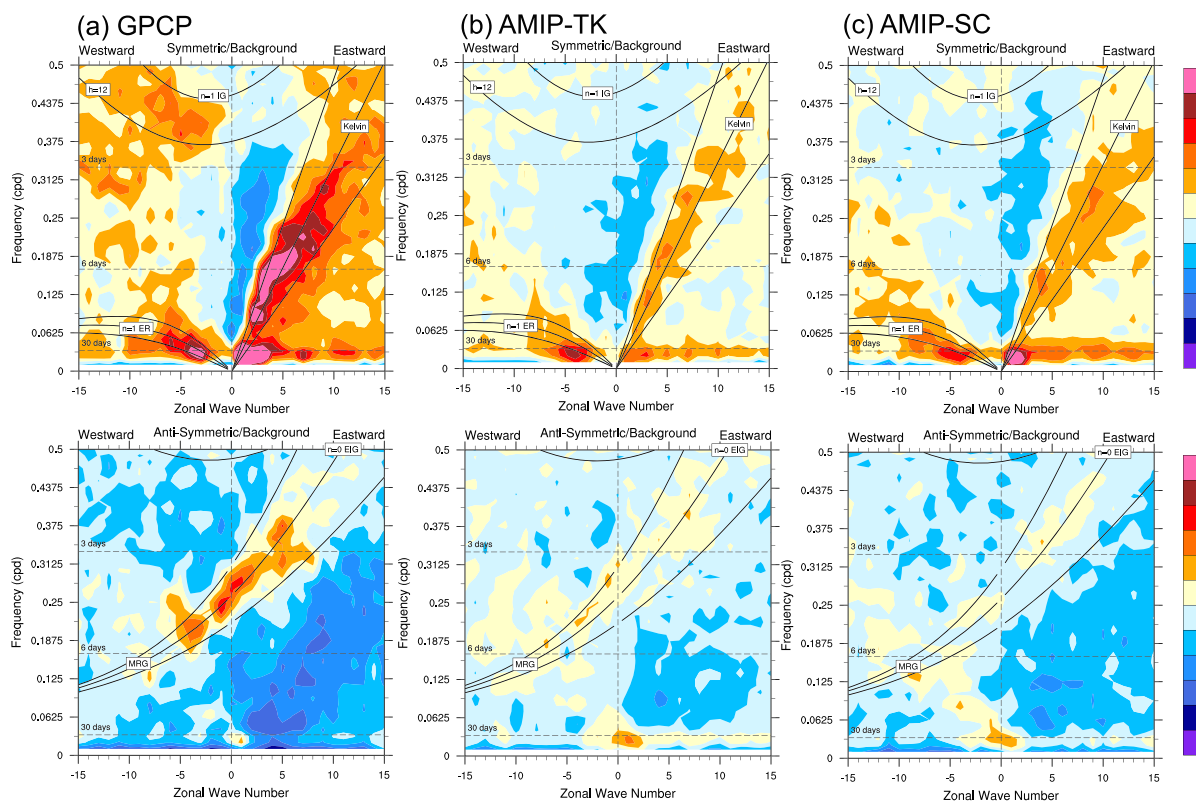


Figure 7. (a–c) Wavenumber-frequency power spectra of the symmetric (upper row) and antisymmetric (lower row) component of precipitation. Daily GPCP data (1997–2006) were used as the reference.

stronger convection over land in the tropics. Other mean states simulated with the SC scheme are basically comparable or better than the TK scheme.

4.3. Tropical Variability

The simulated tropical variability was investigated in terms of interannual and intraseasonal time scales. For interannual variability, the atmospheric response to ENSO was evaluated by regression analysis of monthly precipitation anomalies onto the Niño 3.4 index (Figure 6). In both simulations, positive regression over ITCZ was well reproduced, but a too strong positive value continues to appear from the western to eastern Pacific in both model results. As seen in the trends of AMIP-TK in the western Pacific region, the precipitation response to the SST anomaly of Niño 3.4 index is worse than that of AMIP-SC because the negative regression coefficients are missing in the western Pacific in AMIP-TK. In the Indian Ocean, an almost neutral precipitation response was observed in the observation, but both cases simulated stronger negative or positive patterns in the region. In the Atlantic Ocean, AMIP-TK simulated a better negative response compared to AMIP-SC over the ocean, but the negative response was too strong around the northern part of South America. In the SPCZ region, both simulations failed to simulate a negative precipitation response. The results of these trends show that the improvement due to the SC scheme is considered to be limited to the Pacific Ocean.

The intraseasonal variability of the atmosphere is dominated by CCEWs and the MJO. Their signals were analyzed using wavenumber-frequency spectra of daily precipitation in the tropics (Figure 7). As reported by Crueger et al. (2018), AMIP-TK simulated generally weaker Kelvin and inertia-gravity wave signals than observed and the MJO signal was lacking in the symmetric components. Also AMIP-SC suffered from overly weak Kelvin and gravity wave signals, whereas the MJO signals are considerably more pronounced at eastward moving Wavenumbers 1 and 2. Considering the antisymmetric components, both cases simulated mixed Rossby-gravity wave signals, although the signals are once again weaker than observed. These results are unlike those of Baba (2019), who reported larger-amplitude wave signals, apparently due to differences in other aspects of model formulation. Hence, this may be due to other physical parameterizations than the

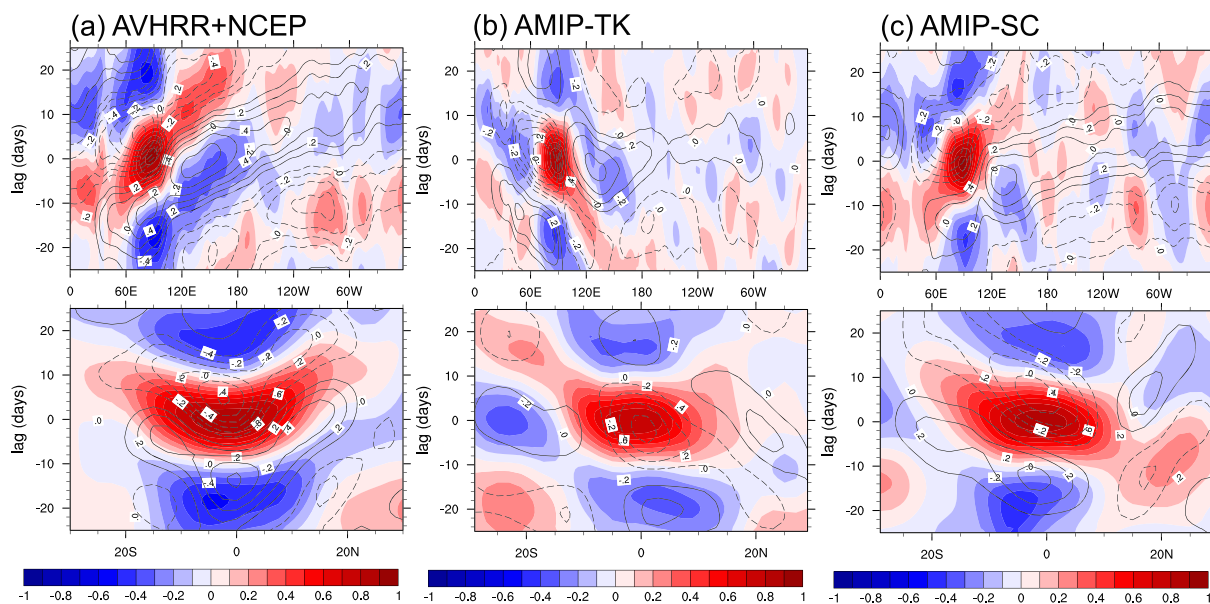


Figure 8. (a–c) Lag-longitude (upper row) and lag-latitude (lower row) correlation diagrams for all seasons. Shade and line correspond to anomalies of OLR and zonal wind at 850 hPa, respectively.

convection scheme, such as partial condensation in a nonconvective cloud scheme and a planetary boundary layer scheme that consider subgrid-scale moisture variation.

Simulated features of the MJO were analyzed using the U.S. Climate and Ocean: Variability, Predictability and Change (CLIVAR) MJO diagnostics (Waliser et al., 2009). Anomalies of OLR and wind components from daily climatologies were used to diagnose the MJO, while Advanced Very High Resolution Radiometer (AVHRR) data (Liebmann & Smith, 1996) and National Centers for Environmental Prediction (NCEP)/National Center for Atmospheric Research (NCAR) reanalysis data (Kalnay et al., 1996) were used for the reference. Lag-longitude and lag-latitude correlation diagrams for the anomalies of simulated OLR and zonal wind at 850 hPa are compared in Figure 8. The observed case shows that MJO-related signals propagate eastward in longitude and poleward in latitude. The eastward propagation is entirely missing in AMIP-TK, where the OLR and zonal wind anomalies propagate westward in the longitude. In contrast, AMIP-SC shows eastward propagating signals similar to what is observed, although the model signals are somewhat weaker, especially to the east of the Maritime Continent. In the lag-latitude diagrams, both cases simulated weaker northward propagation compared to the observations.

Based on Wheeler and Hendon (2004), a combined empirical orthogonal function (EOF) analysis was performed for the OLR, zonal wind at 850 hPa (U850), and zonal wind at 200 hPa (U200). Computed EOFs are compared in Figure 9. The first and second EOFs (EOF1 and EOF2) explain 24.7% of the variances in AMIP-TK and 33.2% of the variances in AMIP-SC, respectively, and are well separated from the remaining EOFs, based on the criterion of North et al. (1982). Comparison of the first two leading EOFs shows that their percentage of explained variance is smaller in the model than in observation, especially in the case of AMIP-TK. Moreover, peaks of OLR, U850, and U200 were not qualitatively reproduced in the EOF2.

To understand the comprehensive differences in intraseasonal variability, life cycle composites of MJO were computed and compared (Figure 10). Principal components (PCs) computed from the combined EOF analysis were used to identify each corresponding phase of the MJO. The comparison suggests that AMIP-SC represents better composited MJO features and better strength of OLR anomaly signals than AMIP-TK. In AMIP-TK, the OLR signal is very weak, and moreover, no eastward propagating organized structures are observable. This is because the first and second PCs (PC1 and PC2) do not form an eastward propagating pair (Waliser et al., 2009). Although AMIP-SC simulates better MJO features, the appearance and eastward propagation of the signals of AMIP-SC are shifted slightly earlier than the observation in the MJO phases, suggesting that there might be a deviation between the phases and variability of AMIP-SC and the observations.

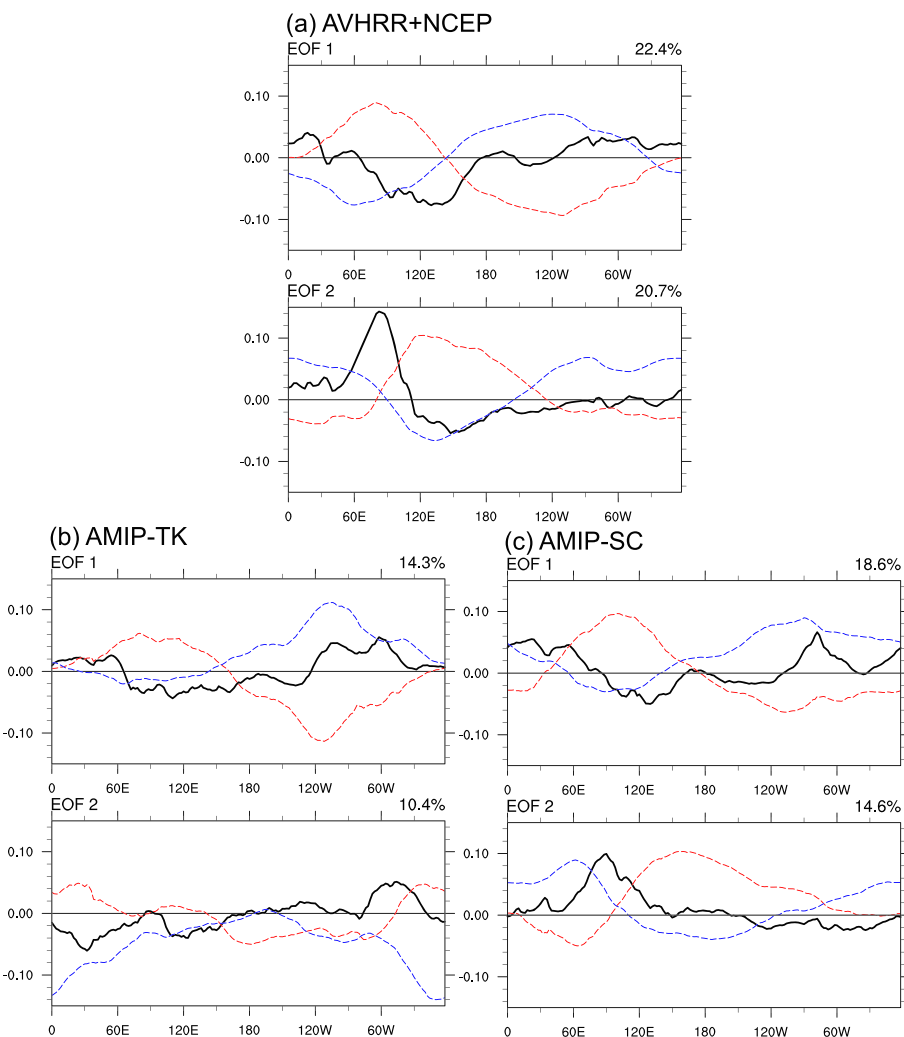


Figure 9. (a–c) The first and second combined EOF modes (EOF1 and EOF2) for all seasons. Thick black, thin dashed red, and thin dashed blue lines correspond to anomalies of OLR, zonal wind at 850 hPa (U850), and zonal wind at 200 hPa (U200), respectively. The percentages indicated in each panel are the variances explained by the respective EOFs.

5. Analysis on Intraseasonal Tropical Variability

5.1. Sensitivity Experiments

The results shown above indicate that AMIP-SC simulates the MJO better than AMIP-TK. However, several different parameterizations were employed in the two schemes as described in section 2.2, and thus, impacts of each parameterization on the reproducibility of MJO remain unknown. To clarify the impacts, two additional sensitivity experiments using modified SC schemes were performed. The modified schemes are (1) SC scheme with the number of cloud types reduced from 14 to 1 (SCS scheme hereafter) and (2) SC scheme with the same convective closure as in the TK scheme (SCC scheme hereafter). In the configuration of the SCS scheme, cloud base updraft velocity was set to 1 m/s. The SCS and SCC schemes are used to reveal the impacts of spectral representation and convective closure, respectively. Additional experiments using these modified schemes are referred to as AMIP-SCS and AMIP-SCC, respectively, hereafter. The TK and SC schemes are different in terms of their shallow convective closures, as the cloud base mass flux is diagnosed by moisture tendency (TK scheme) or MSE tendency (SC scheme). However, as Chikira (2014) described, MSE is dominated by moisture variation during the MJO development, and our preliminary experiments indicated that the difference had small impacts; thus, the comparison for the difference in shallow convective closures is omitted here.

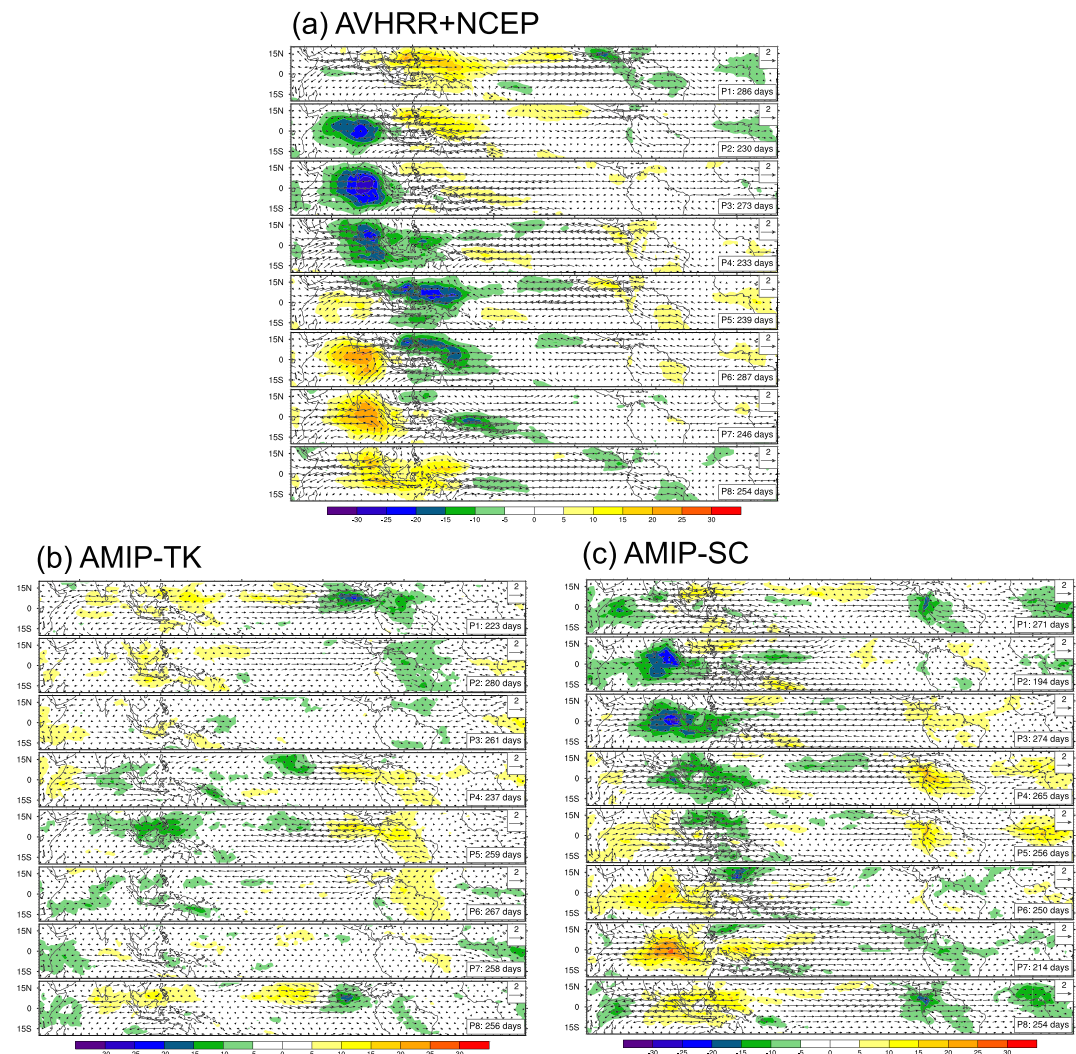


Figure 10. (a–c) Life cycle composites of MJO for all seasons. The 20- to 100-day band-pass-filtered OLR (shading: W/m^2), zonal and meridional winds at 850 hPa (vectors: m/s) anomalies were used. The phase and number of composited days are indicated in lower right corner of each panel.

The intraseasonal variability of both sensitivity cases was evaluated using identical analysis procedures as in section 4.3. The wavenumber frequency spectra of daily precipitation (Figure 11) apparently shows that the signals of equatorial Kelvin, mixed-Rossby gravity waves and also MJO became weaker compared to AMIP-SC. This fact indicates that use of SCS or SCC scheme results in weaker tropical variability. The diagrams of lag-longitude and lag-latitude (Figure 12) indicate that AMIP-SCS and AMIP-SCC partly reproduce eastward propagating structure both in the OLR and U850, while eastward (and poleward) propagating trend of OLR as well as zonal wind anomalies slightly became obscure compared to AMIP-SC, and AMIP-SCC shows more obscure eastward propagating trends. In the combined EOF analysis (Figure 13), AMIP-SCS and AMIP-SCC are found to simulate similar EOFs patterns compared to AMIP-SC and AMIP-TK, respectively. Similar to AMIP-TK, PC1 and PC2 simulated by AMIP-SCC did not form an eastward propagating pair (not shown here). AMIP-SCS simulated similar PCs as AMIP-SC did, but its explained variances are smaller than for AMIP-SC. To evaluate the mean state of the sensitivity cases, we performed standardized error analysis. The error values of AMIP-SCS and AMIP-SCC are found to be 1% smaller and 8% larger than that of AMIP-SC, respectively. In addition, to quantitatively evaluate MJO fidelity of all cases, we calculated MJO scores based on Crueger et al. (2013). The MJO scores are better in the order of AMIP-SC,

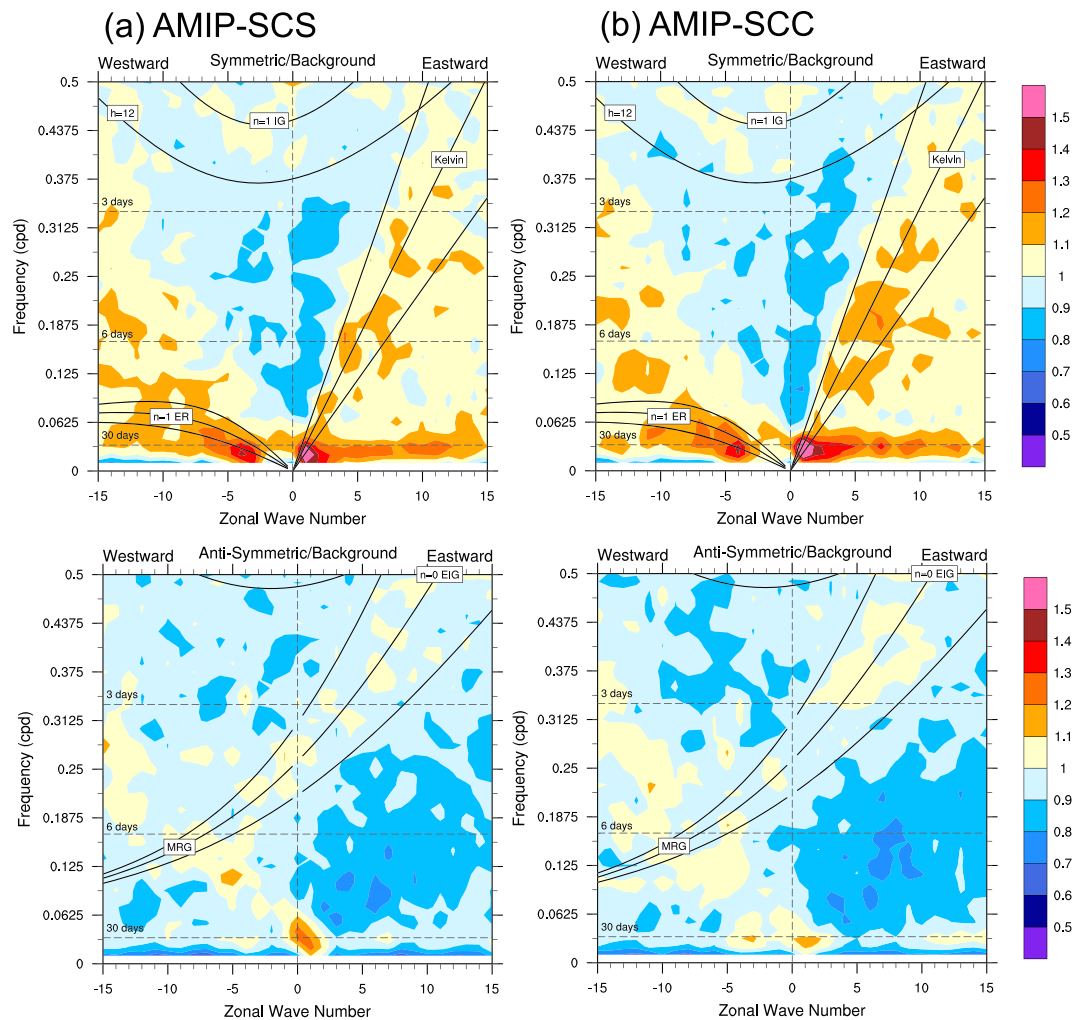


Figure 11. As Figure 7 but for AMIP-SCS and AMIP-SCC.

AMIP-SCS, AMIP-SCC, and AMIP-TK (Appendix B). The above analysis suggests that both the spectral representation and the density-weighted CAPE closure are necessary with the entrainment parameterization for reproducing better intraseasonal variability.

5.2. Composed Fields

To extract the representative structure of the MJO's organized convection and understand the influence of convection schemes on the structure, the composite method of Chikira and Sugiyama (2013) is used in the following analysis. In this method, filtered daily OLR anomalies are used to detect the location of the MJO. The daily OLR anomalies were filtered in Zonal Wavenumbers 1–5, band-pass filtered for 20–100 days, and latitudinally averaged between 10°S and 10°N. The MJO signal was identified by the minimum value of OLR less than -0.7σ , where σ is the standard deviation of filtered OLR anomaly, and the location of the MJO to be detected was limited between 60°E and 150°W. In the original method, MJO signal that could not propagate longer than 60° in longitude was removed from the detection. However, the simulated MJOs of our experiments were found to have shorter lifetime as seen in the former analysis (e.g., Figures 8 and 10); thus, the threshold of propagation longitude was changed; that is, a minimum zonal propagation distance of 40° in longitude was basically used for the following results. Although the threshold value was relaxed, AMIP-TK simulated only few eastward propagating waves as the EOF analysis could not capture the waves well; thus, the threshold was further relaxed as 20° in the longitude. Regarding the day when the minimum OLR appeared in each longitude as 0 relative day, latitudinally averaged fields between 10°S and 10°N in each longitude were composited for –30 to 20 relative days (denoted as Day –30 to Day +20, hereafter). The

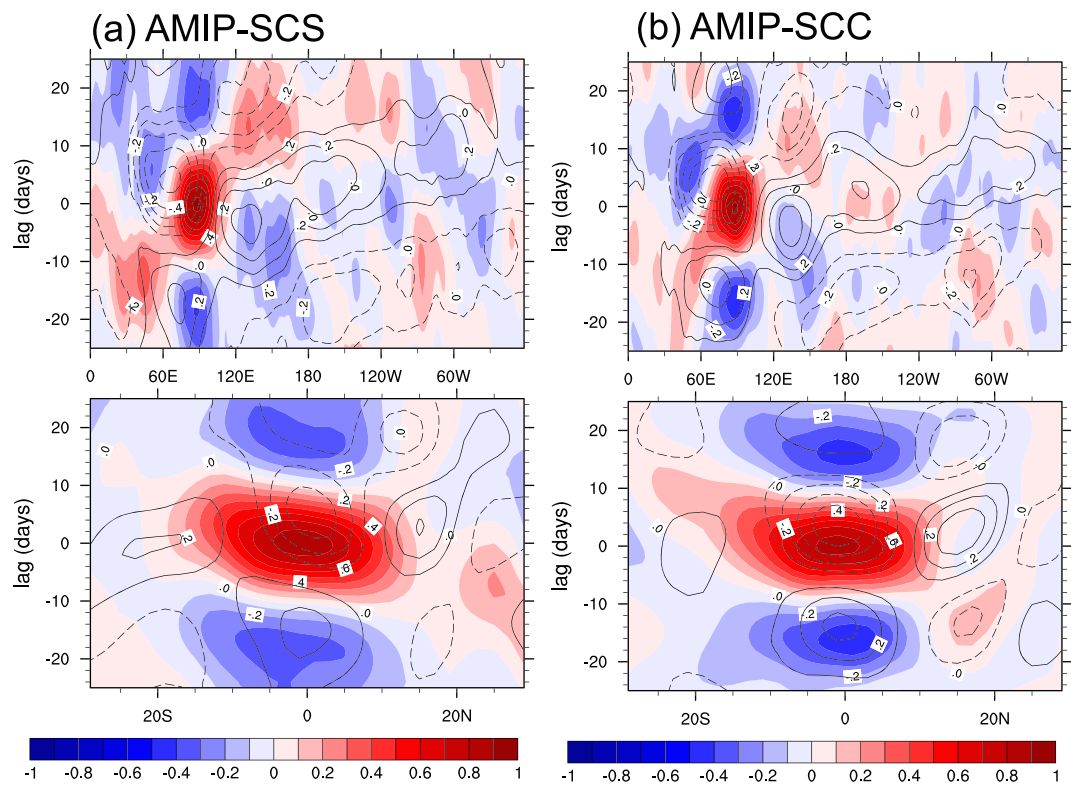


Figure 12. As Figure 8 but for AMIP-SCS and AMIP-SCC.

anomalies of each variable are defined as departures from the time mean values averaged from Day -30 to $+20$, hereafter.

Since AMIP-SC showed the best results in simulating the MJO, analyzing the deviation of temperature and humidity-related fields in the other cases from those of AMIP-SC may help understanding why the other cases performed less well for the MJO (Figure 14). AMIP-TK simulates strong warmer and drier (indicated

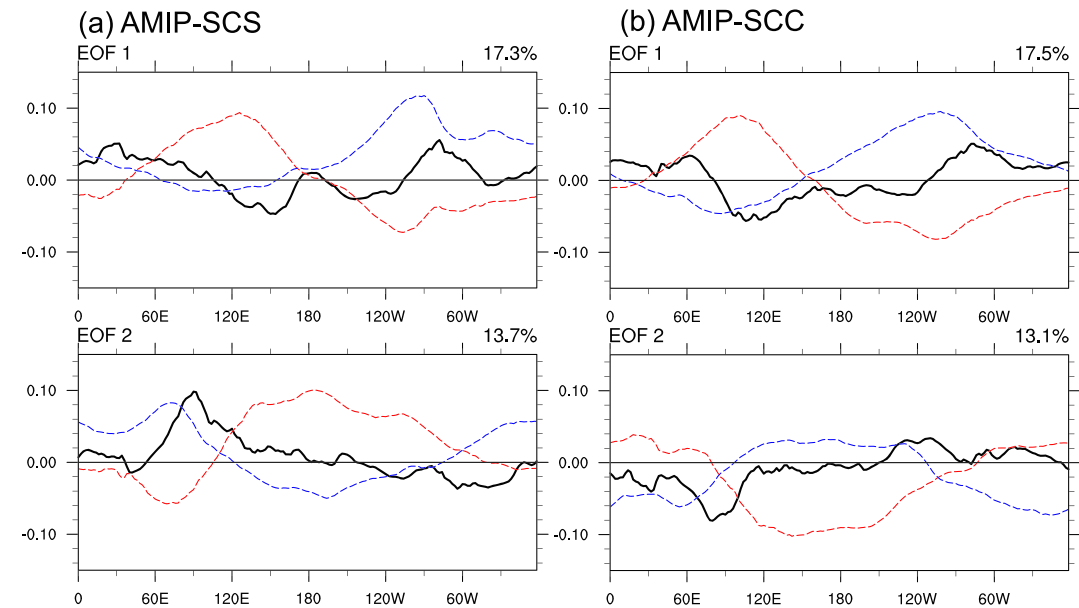


Figure 13. As Figure 9 but for AMIP-SCS and AMIP-SCC.

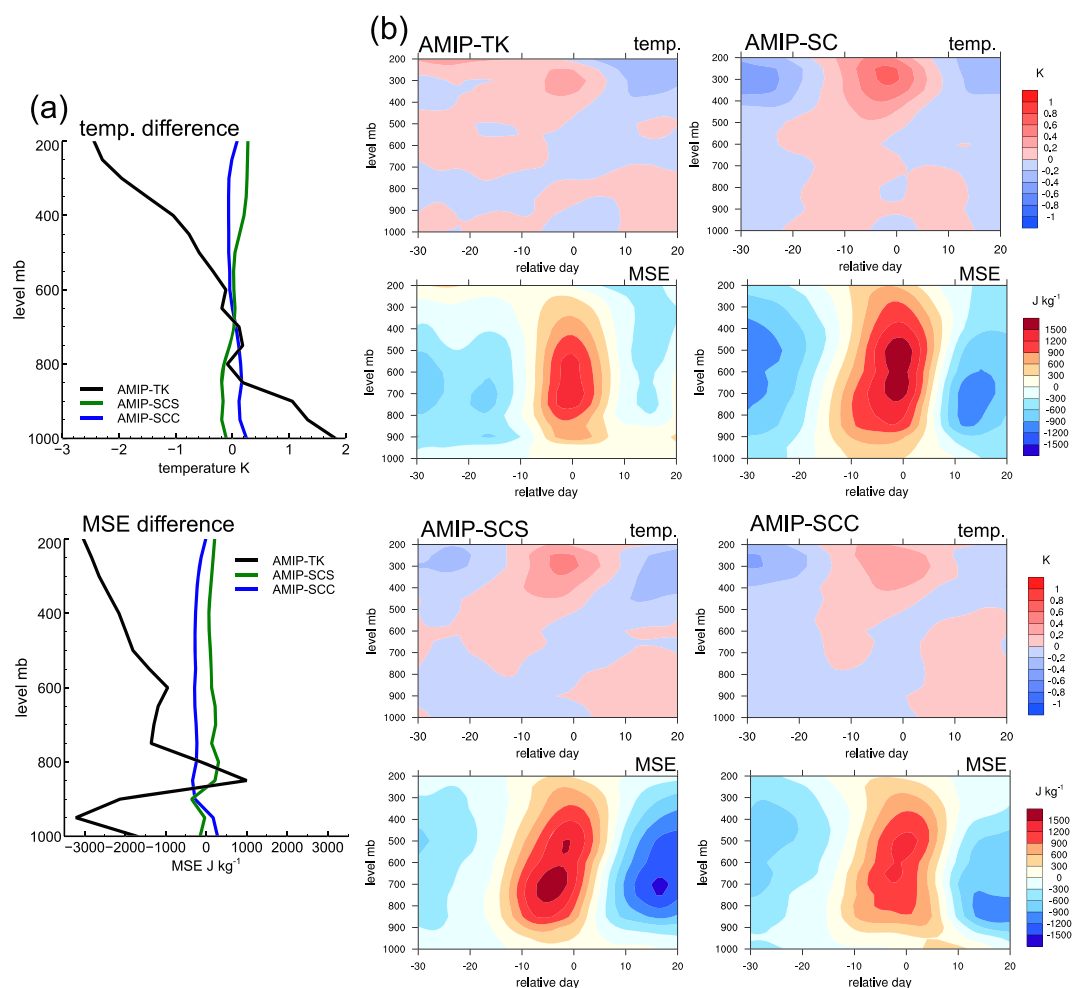


Figure 14. Composited vertical profiles of time mean and anomaly for temperature and MSE. (a) Difference of vertical profiles of time mean from AMIP-SC for (top) temperature and (bottom) MSE. (b) Vertical profiles of (top) temperature and (bottom) MSE anomalies.

by low MSE) conditions below the 800-mb level except for the MSE peak in 800-mb level in the time mean profile. Note that this case shows warmer and drier conditions in the low levels even in the comparison to observations (not shown here). This trend in AMIP-TK is considered to derive from dominant shallow convection, since shallow convection warms the lower atmosphere and consumes moisture in the low levels. Similar but weak warmer and drier conditions in the lower levels are observed in the time mean profile of AMIP-SCC, while slightly colder and wetter conditions in the lower levels are observed in the time mean profile of AMIP-SCS. Considering anomaly profiles, except for AMIP-TK, significances of the time mean and anomalous temperature are found to be comparable each other and less significant than the MSE anomaly. The MSE anomaly indicates that except for AMIP-TK, the MSE anomaly is more significant than the time mean, meaning that AMIP-SCS simulated drier condition after Day +10, and AMIP-SCC simulated drier condition around Day 0 than AMIP-SC. AMIP-TK simulated smaller MSE anomaly than other cases, and the anomaly is less significant than the time mean. Consequently, in AMIP-TK, it can be assumed that time mean (background) atmospheric condition was much affected by dominant shallow convection, and the significance was much greater than anomalous fields originating from the organized convection.

Figure 15 shows composited convective heating profiles by deep and shallow convection. Here, based on Bechtold et al. (2014), each convection was identified by the convection depth; that is, convection depth less than 200 hPa is identified as shallow convection and, otherwise, identified as deep convection for simplicity. In the cases of SC and SC-derived schemes, internal unresolved cloud types were categorized following

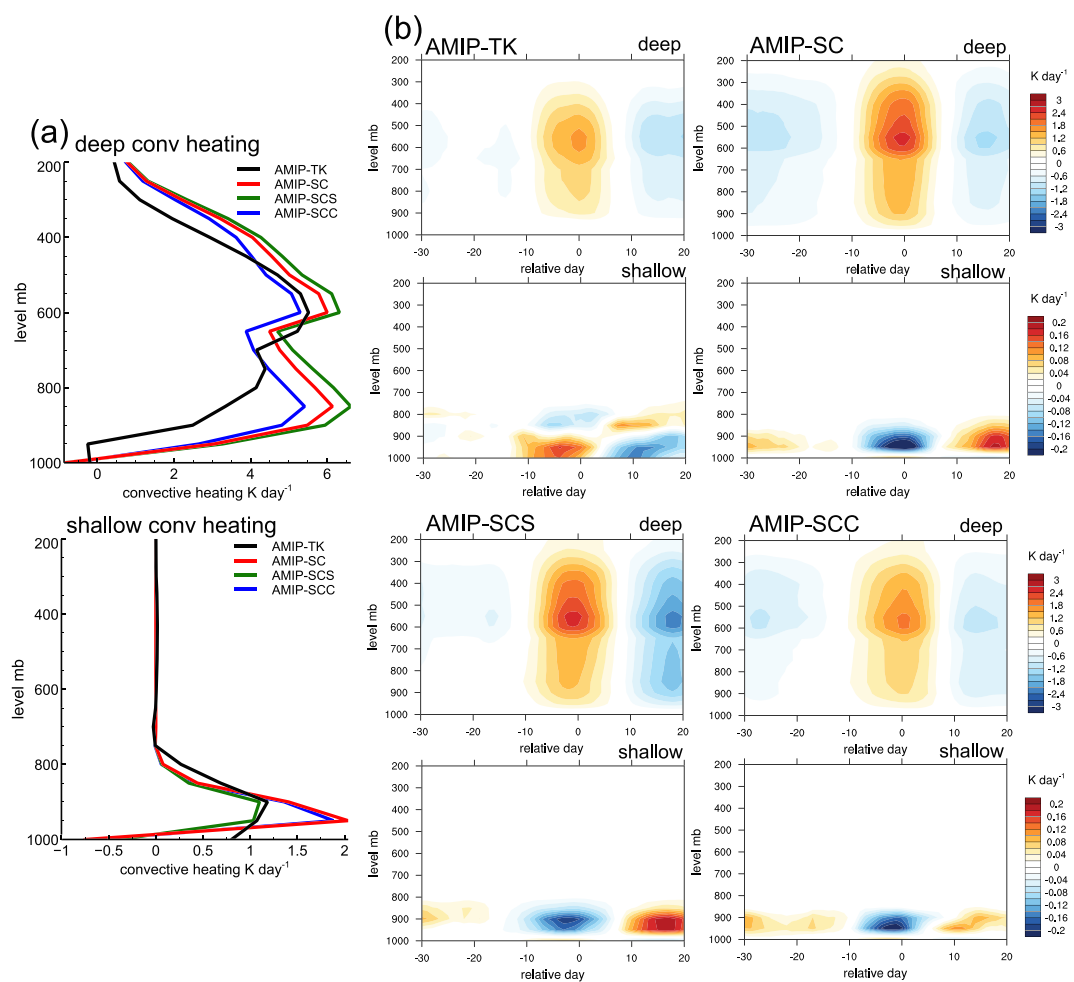


Figure 15. Composited vertical profiles of time mean and anomaly for convective heating. (a) Vertical profiles of time mean convective heating for (top) deep convection and (bottom) shallow convection. Vertical profiles of anomalous convective heating for (top) deep convection and (bottom) shallow convection.

this criterion. AMIP-TK apparently shows weaker time mean heating by both deep and shallow convection than AMIP-SC and also shows weaker anomalous heating by deep convection than AMIP-SC. Since AMIP-TK is considered to simulate warmer and drier time mean atmospheric condition due to the dominant shallow convection, this result indicates that the convection is suppressed or much diluted by more entrainment in the convection. In the sensitivity cases, all the cases simulated negative anomalous heating by shallow convection when positive anomalous heating by deep convection appears. This means that significance of shallow convection is weakened when organized convection appears. This feature is not observable in AMIP-TK. In addition, in these cases, the time mean heating is more dominant than anomalous heating for shallow convection (only the time mean heating will be mentioned for shallow convection, hereafter). Comparing with AMIP-SC, AMIP-SCS simulated comparable time mean and anomalous heating by deep convection but simulated large negative anomalous heating after Day 0 and weaker heating by shallow convection. This may be due to the lack of shallow clouds that supply moisture upward, since the spectral representation for convective clouds is removed in this case. AMIP-SCC simulated weaker time mean and anomalous heating by deep convection from low to upper levels but simulated comparable heating by shallow convection. Because the convective closure for deep convection of this case was changed from AMIP-SC, the difference in the closure is assumed to degrade the feature of deep convection.

Figure 16 compares entrainment profiles by deep and shallow convection. In the time mean profiles, it is apparently shown that AMIP-TK simulated much larger entrainment in the shallow convection than other cases, and the heights of maximum entrainment are separated between deep and shallow convection. On

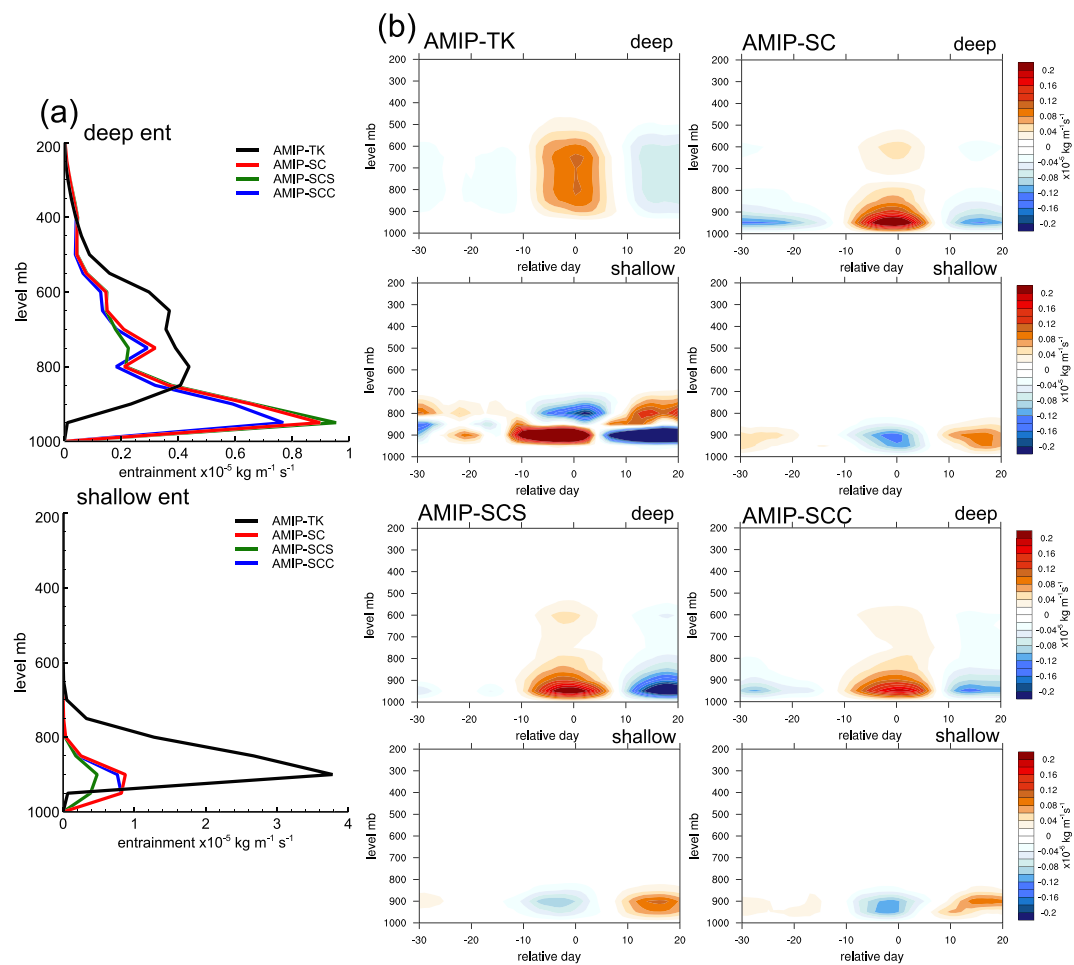


Figure 16. As Figure 15 but for entrainment.

the other hand, the heights of maximum entrainment are overlapped when SC and SC-derived schemes are used. Since the difference is observed regardless of spectral representation and convective closure, difference in the entrainment parameterizations is considered to cause the difference. In the sensitivity cases, AMIP-SCS simulated smaller entrainment than other cases in the shallow convection. On the other hand, AMIP-SCC simulated largely similar entrainment to AMIP-SC but simulated smaller entrainment for deep convection in the low level. These trends correspond to their weaker convective heating in the low level shown in Figure 15, meaning that weaker convective activities in the low level than AMIP-SC. The anomaly profiles indicate that they basically correspond to anomalous convective heating, but small entrainment correspond to large convective heating of deep convection in the upper level, except for AMIP-TK. Since deep convection generally has smaller entrainment than shallow convection (Baba, 2019), the SC and SC-derived schemes seem to successfully suppress excessive increase of entrainment for the deep convection in contrast to the TK scheme. Considering these results, the impact of SC scheme's entrainment parameterization is found to suppress excessive increase of entrainment and is able to simulate continuous entrainment profiles across deep and shallow convection. In particular, the latter feature may be originated from the unified entrainment parameterization that can be applied to both deep and shallow convection.

5.3. Moisture Variation

To reveal what caused the differences in the MJO fidelity of the different cases, further analysis was conducted for convective activities. Moisture variation was chosen here to represent MJO-related convective activity, and its budget was analyzed in detail. For this analysis, the identical composite method described in section 5.2 was used. The resulting composited specific humidity anomalies are compared in Figure 17. The composited profiles of observations clearly capture organized MJO-related humidity anomalies, which

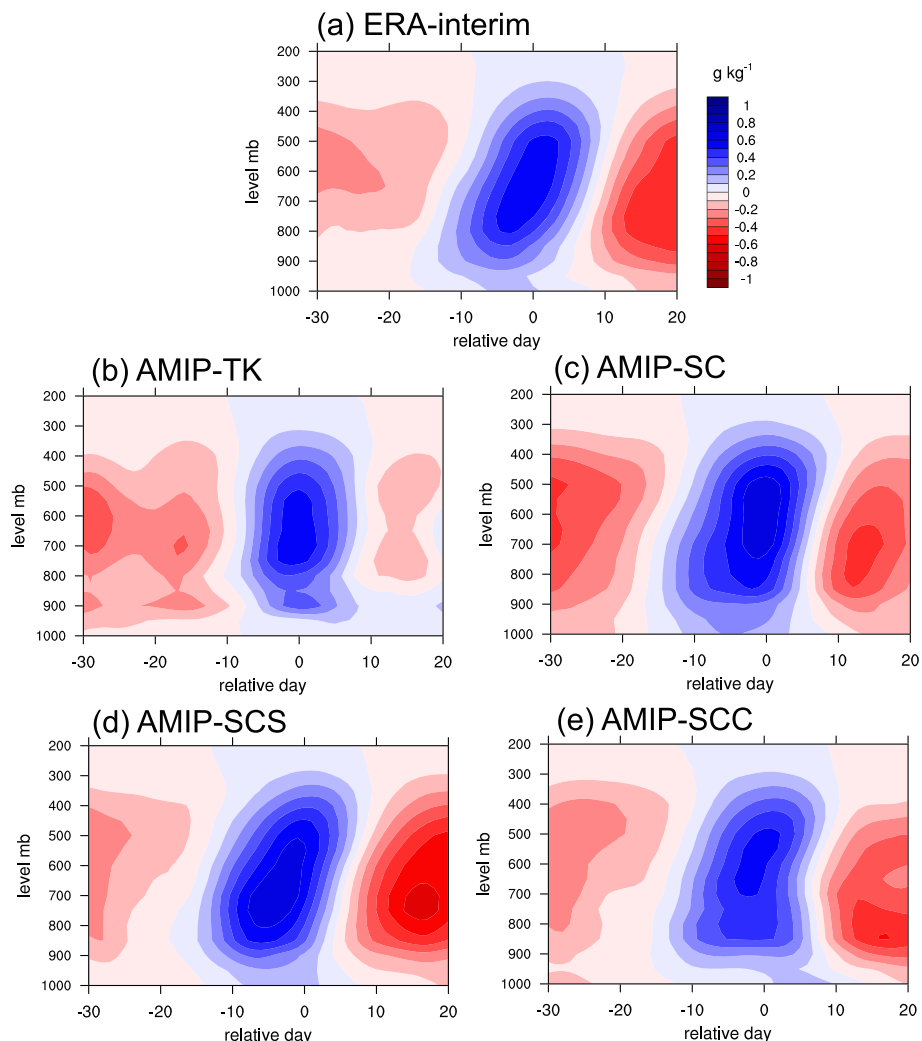


Figure 17. (a–e) Composed vertical profiles of specific humidity anomalies. The positive and negative values are colored by blue and red shades, respectively.

propagated upward as the positive anomaly (blue colored shade) appears, followed by the negative humidity anomaly (red colored shade). AMIP-TK partly captures an organized structure, but the organized structure is different from the observation as the structure is more upright and the positive amplitude seems to have shorter lifetime. AMIP-SC successfully simulates the organized structure, and the features are similar as seen in the observation. The sensitivity cases succeeded in simulating similar humidity anomalies, but AMIP-SCS simulated larger negative amplitude after Day +10, and AMIP-SCC simulated smaller positive amplitude around Day 0 compared to the observation.

From the analysis of the MJO using reanalysis data and model result, Chikira (2014) (CK14 hereafter) revealed that the net effect of vertical advection and physical processes amplifies a positive humidity anomaly, whereas horizontal advection contributes to eastward propagation of the humidity anomaly. Composed tendencies of specific humidity are compared in Figure 18. In the total moisture tendency of AMIP-SC, positive tendencies appear earlier than the peak of the positive anomaly, which is consistent with the results of CK14. This trend is partly reproduced in the AMIP-TK, but the contrast between positive and negative tendencies is weaker. Similar to CK14, horizontal advection tendencies in AMIP-SC decrease humidity and do not contribute to the increased positive humidity anomaly in the lower troposphere. On the other hand, AMIP-TK shows positive tendencies at both upper and lower levels, except for around 900-mb

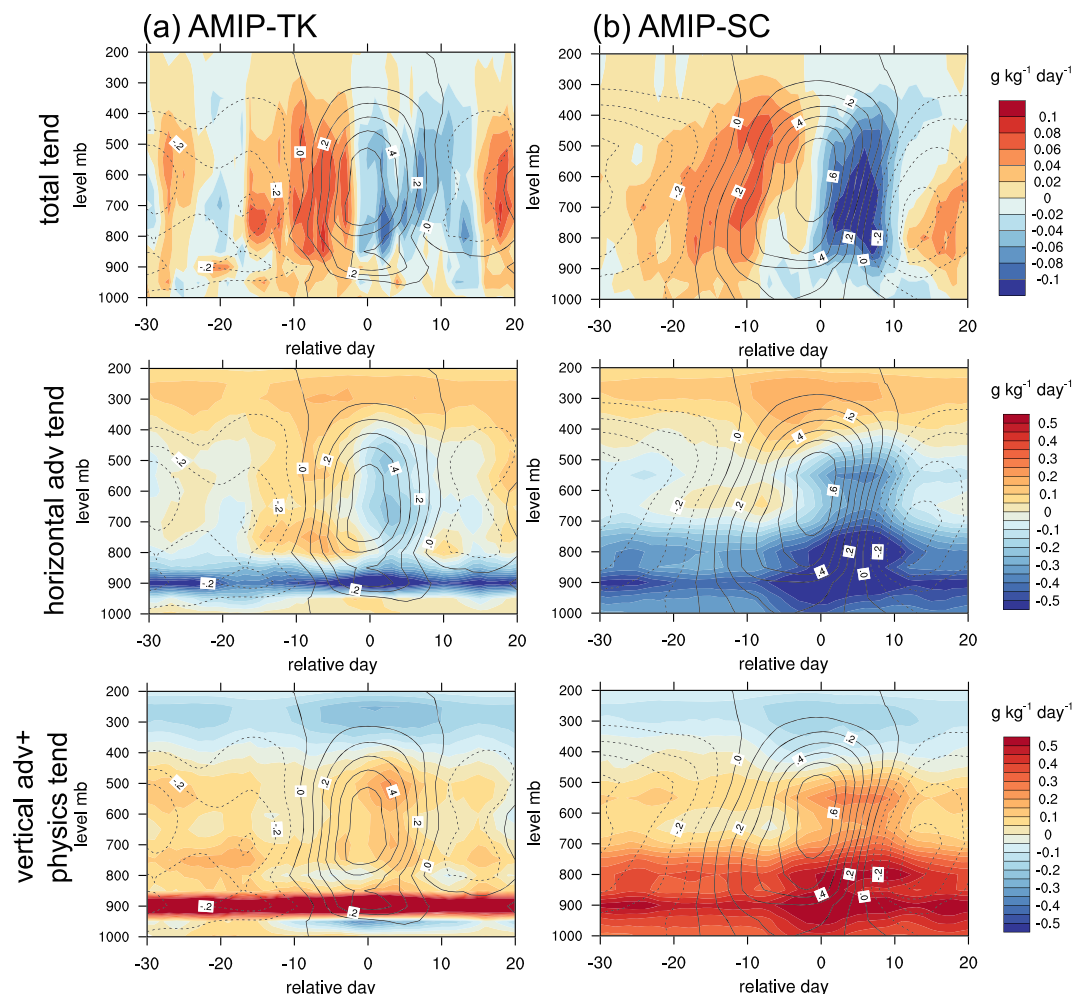


Figure 18. (a, b) Composed vertical profiles of (top row) total, (middle row) horizontal advection, and (bottom row) vertical advection and physics tendencies for specific humidity. Superimposed contour lines are specific humidity anomalies (contour interval is 0.1 g/kg, solid and dashed lines indicate positive and negative values, respectively). The tendencies for AMIP-SCS and AMIP-SCC are omitted for simplicity.

level. The vertical advection and physics tendencies of AMIP-SC clearly show that the increase in humidity is mainly caused by these tendencies, which is consistent with findings of CK14. However, the tendencies of AMIP-TK show different features, which indicate strong positive tendency only at lower levels throughout all days. These findings suggest that the TK scheme may be unable to increase humidity sufficiently at higher altitude by the vertical advection and the physical processes.

Those differences might be derived from different features of tendencies from physical processes. It is hard to distinguish which physical process affects the amplification of humidity and its interaction with the vertical advection. Thus, CK14 proposed a simplified equation to describe the tendency of humidity anomaly only from the tendencies of physical processes, as follows:

$$\left(\frac{\partial q}{\partial t} \right)_{col} \approx (\alpha - 1) (\tilde{C} - \tilde{R}_v) + \frac{\alpha}{L_v} (Q_r + \tilde{Q}_i + Q_{df}) + D_q + S_{df} + S_{hf}, \quad (13)$$

where q is the specific humidity, col indicates a column process (net effect of the vertical advection and the cloud processes for moistening or drying), \tilde{C} is the condensation rate, \tilde{R}_v the reevaporation rate, L_v the latent heat release of condensation, Q_r the radiative heating rate, \tilde{Q}_i the heating rate by liquid-ice transition, Q_{df} the heating rate by vertical diffusion, D_q the q tendency by detrainment, and S_{df} the q tendency by vertical diffusion. The tildes denote the mean value in the environment and α is the nondimensional parameter

that represents significance of moistening or drying by external forcing (i.e., adiabatic forcing by vertical transport), given as

$$\alpha = -L_v \left(\frac{\partial \langle q \rangle}{\partial z} \right) \left(\frac{\partial \langle s \rangle}{\partial z} \right)^{-1}, \quad (14)$$

where s is the dry static energy, the brackets indicate the value is low-pass filtered for more than 20 days and S_{hf} is the high frequency waves of vertical advection given as

$$S_{hf} = -\langle \tilde{\omega} \rangle \frac{\partial q'}{\partial p} - (\tilde{\omega})' \frac{\partial \langle q \rangle}{\partial p} - (\tilde{\omega})' \frac{\partial q'}{\partial p}, \quad (15)$$

where ω is the vertical velocity and $\tilde{\omega} = \omega + \omega_c$ where ω_c is the compensative vertical velocity due to convection. The primes indicate the deviation from the low-pass-filtered values. In equation (13), vertical velocity is replaced by the tendencies that affect vertical advection using weak temperature gradient approximation (Sobel et al., 2001). Thus, the increase in humidity can be explained only by tendencies, excluding vertical advection, especially the dominant slow mode component. Note that almost identical equation to the equation (13) can hold for MSE (Chikira, 2014).

The anomalous tendency of the column process, which is necessary to analyze the budget of the humidity anomaly can be obtained by decomposing the terms in the equation (13) into time mean and anomalous values, and linearising the resulting equation as (Chikira, 2014)

$$\begin{aligned} \left(\frac{\partial q}{\partial t} \right)'_{col} &= \underbrace{\left[(\bar{\alpha} - 1) (\tilde{C}' - \tilde{R}'_v) + \alpha' (\tilde{C} - \tilde{R}_v) \right]}_{\text{first term}} \\ &\quad + \underbrace{\frac{1}{L_v} \left[\bar{\alpha} (Q'_r + \tilde{Q}'_i + Q'_{df}) + \alpha' (\bar{Q}_r + \tilde{Q}_i + \tilde{Q}_{df}) \right]}_{\text{second term}} + \underbrace{(D'_q + S'_{df} + S'_{hf})}_{\text{third term}}, \end{aligned} \quad (16)$$

where the bar and the prime indicate time mean and anomaly redefined as a departure from the time mean. Figure 19 shows the anomalous humidity tendency and anomalous profiles of each term in the equation (16). In the profiles of AMIP-SC, the first term amplifies the humidity anomaly in the midlevel, while the second term amplifies the anomaly in the low to middle levels around Day 0. Since the value of α is generally less than 1 at upper levels, the moistening by the first term is due to reevaporation there. The moistening by the second term is mainly due to radiative heating, which will be further discussed later. The third term works as moistening in the midlevel before Day 0, drying and moistening again in the low level after Day 0. As the results of these tendency profiles, large anomalous column process tendency appears between Days 0 and +10. Comparing the results with AMIP-SC, the amplification in AMIP-TK is confined around Day 0, and the main amplification in the low to middle levels is found to be derived from the third term. The second term in this case is only significant below the 700-mb level. In the sensitivity cases, AMIP-SC simulated similar amplification trends, but negative amplification by the third term is significant around Day 0; thus, the total amplification in the column process became smaller than that of AMIP-SC, while positive amplification by the third term is strong during Day -30 to -20. AMIP-SCC simulated much larger amplification at Day 0; however, this case shows strong drying trends after Day 0 by the third term, resulting in shorter amplification time.

Since the first terms show comparable contributions among the cases, the main difference in the moisture amplification is considered to derive from the second and third terms (Appendix C1). The most significant moistening in the second term is caused by longwave radiation (Appendix C2). Nonanomalous tendency profiles by longwave radiation are compared with corresponding profiles of cloud condensate in Figure 20. In all cases, longwave cooling is suppressed at Day 0 and this is caused by large amount of cloud condensate throughout all levels. Due to the larger amount of cloud condensate, emission of longwave radiation toward the top of the atmosphere is prevented, leading to the longwave heating below the clouds. This effect is known to play important roles in the maintenance of the MJO (e.g., Arnold & Randall, 2015; Chikira, 2014; Del Genio & Chen, 2015). AMIP-TK shows less cloud condensate during all relative days and at all levels, because AMIP-TK simulated warmer and drier conditions (Figure 14); thus, the conditions are more

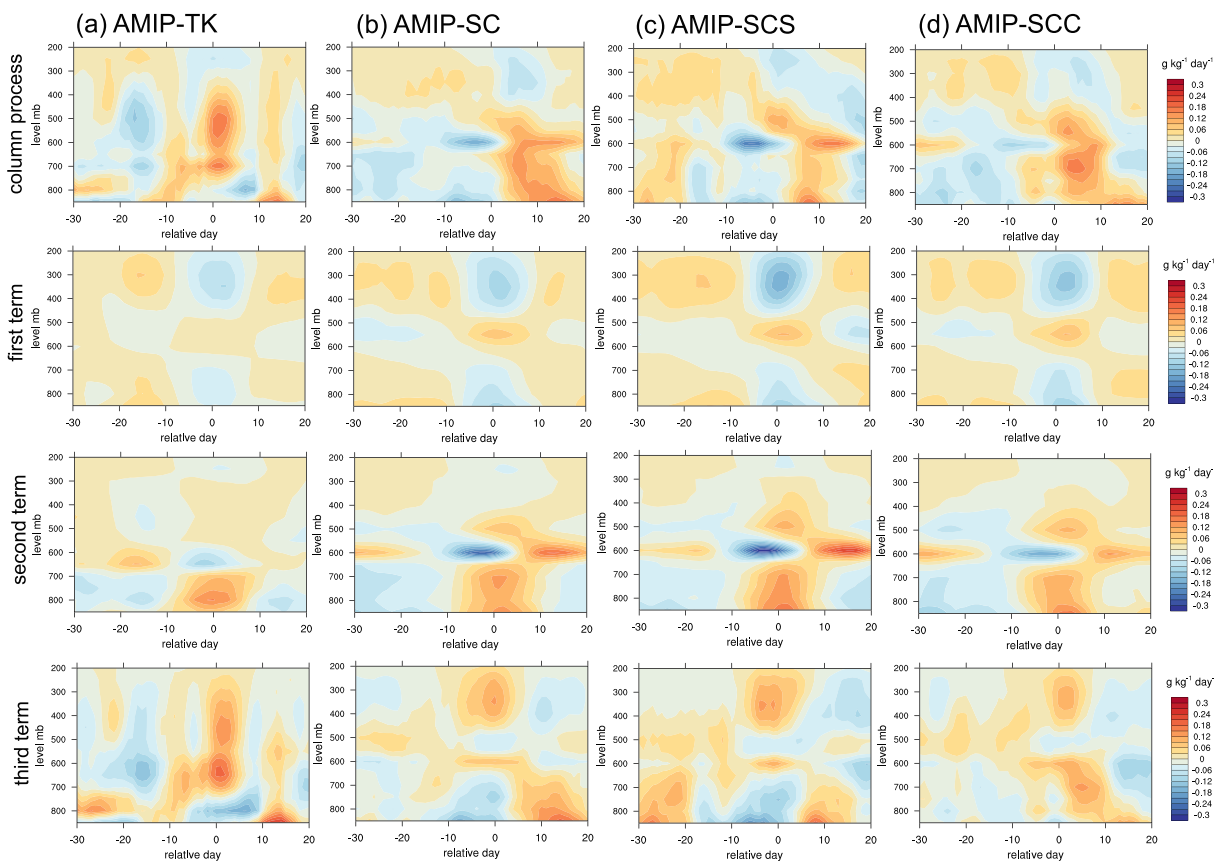


Figure 19. As Figure 18 but for composited anomalous tendencies of specific humidity of (first row) column process and (second to fourth row) anomalous profiles of each term in equation (16). The profiles below the 850-mb level are omitted since α can take significantly large values under statistically unstable atmospheric conditions.

undersaturated and cloud condensate tends to evaporate in this case. As the result of less clouds especially in the midlevel, much longwave cooling occurs, and it causes a stronger drying effect in AMIP-TK. In other cases, such significant longwave cooling is not observed, but AMIP-SCS lacks cloud condensate at 400-mb level between Days +10 and +20, and more drying appears there. This is related to the fact deep convection of this case is lacking after Day 0 as shown in Figure 15. AMIP-SCC simulated less cloud condensate in the midlevel around Day 0 than AMIP-SC, which was derived from the less convective heating of deep convection also as shown in Figure 15. Eventually, AMIP-SCC simulated less moistening by radiation below the midlevel compared to AMIP-SC (Figure 19).

Contributions of each term included in the third term of equation (16) to humidity anomaly are compared in Figure 21. AMIP-TK simulated rapidly increased or decreased detrainment around Day 0, thus simulated shorter amplification time, although AMIP-TK simulated much larger detrainment than AMIP-SC in the low level (Appendix C3). Since the high-frequency waves indicate negative amplification, it also contributed to the shorter amplification time. AMIP-SCS simulated positive amplification by the detrainment in the low levels before Day -20, but it turned to negative amplification between Days -10 and 0, because low-level moisture supply by detrainment is lacking there. AMIP-SCC simulated low negative amplification in the low level around Day 0, and following positive amplification is confined between Days 0 and +10; thus, it results in drying after Day +10 and shorter amplification time. These trends are derived from less detrainment from convection in the low level compared to AMIP-SC (Appendix C3).

After the organized convection appeared, AMIP-SCS and AMIP-SCC simulated less shallow convection and weaker deep convection in the lower levels than AMIP-SC, respectively, and the fact seems to degrade the results of these cases. Therefore, the capability of the scheme to simulate coexisting shallow and deep clouds is considered important for sustaining the MJO sufficiently. Figure 22 shows differences of vertical profiles of cloud mass flux when the deep convection reached at upper (300 mb) and middle (500 mb) levels.

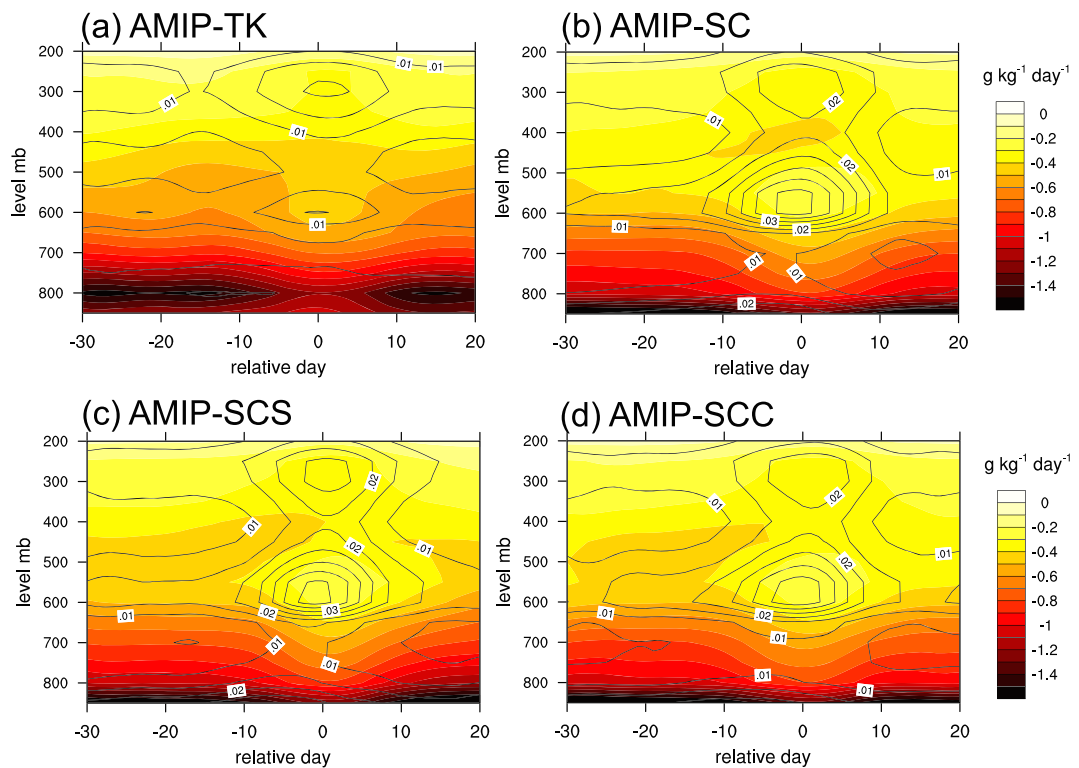


Figure 20. As Figure 18 but for nonanomalous tendencies by longwave heating (cooling) and corresponding cloud condensate. The shades and contour lines indicate tendencies by longwave heating and cloud condensate (g/kg , contour interval is 0.005 g/kg), respectively.

Clear differences are seen in the lower levels where AMIP-SCS and AMIP-SCC simulated less cloud mass flux, which is derived from low-level convective clouds, meaning that upward moisture supply from the sea surface (except over the Maritime Continent) by convective updraft is decreased in these cases. Indeed, low-level entrainment is weak as in the shallow convection of AMIP-SCS and in the low-level part of deep convection of AMIP-SCC (Figure 16). This result regarding the modified SC schemes indicates that simulating shallow convection (or low-level convective cloud) is necessary for sustaining the MJO, even when deep convection appears. On the other hand, since AMIP-TK tends to simulate too much shallow convection, it simulated greater low-level mass flux than AMIP-SC between 800- and 900-mb levels. Notable feature of this case is that positive difference is limited between 800- and 900-mb levels, and other differences show

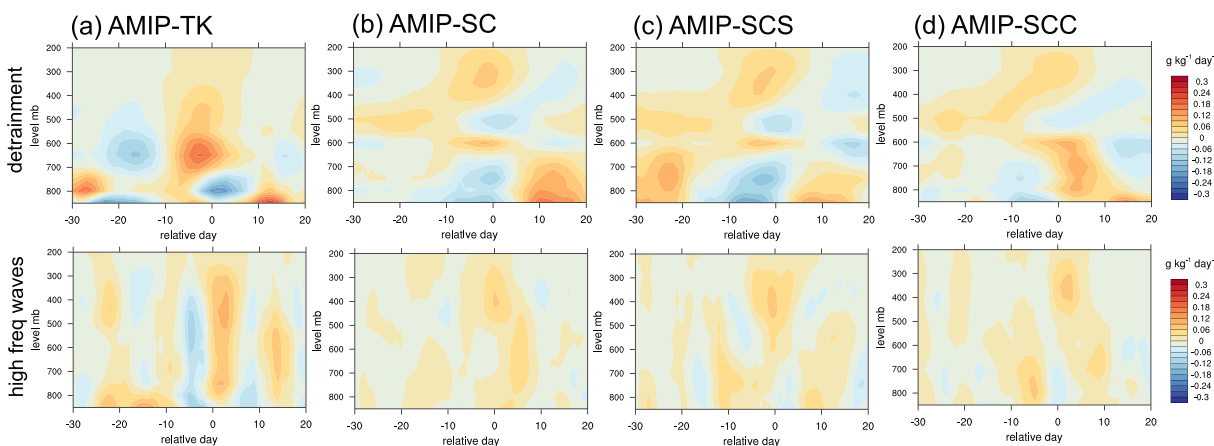


Figure 21. As Figure 18 but for composited anomalous tendencies included in the third term of equation (16). Each panel indicates tendencies by (top) detrainment, and (bottom) high frequency waves.

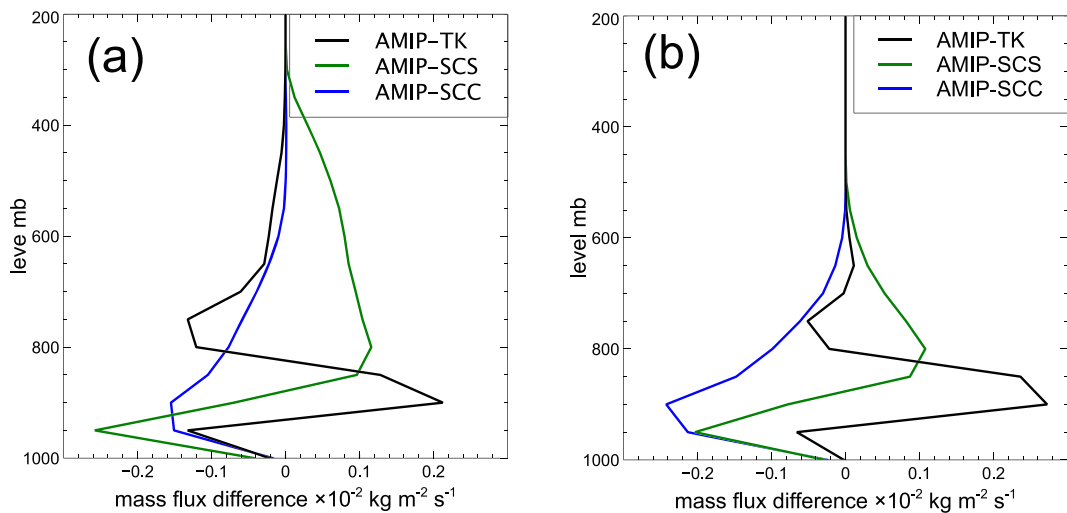


Figure 22. Composited vertical profiles of cloud mass flux between Days 0 and +20. The composite was taken with respect to MJO location and cloud top levels. Each panel indicates (a) difference of cloud mass flux of other cases from AMIP-SC with respect to the cloud top reaching 300-mb level and (b) difference of cloud mass flux of other cases from AMIP-SC with respect to the cloud top reaching 500-mb level. Each cloud mass flux profile is normalized by the number of composited convective columns.

negative difference. Therefore, in AMIP-TK, greater upward moisture transport from the low level is also limited in these levels, meaning that moisture is not supplied well to the deeper convection. This feature is derived from discontinuous entrainment profiles (Figure 16), which is computed by switching entrainment parameterization depending on the bulk cloud type.

The above analysis revealed different features of organized convection simulated by different convection schemes. AMIP-TK preferred warmer and drier conditions when organized convection occurred and simulated weaker organized convection. This result was found to be attributed to too much shallow convection with excessive entrainment. Since the moist condition is apparently desirable to induce organized convection, such opposite dry condition of AMIP-TK was inevitable because of the features of the TK scheme. AMIP-SCS that used only one cloud type and worked as a bulk convection scheme showed a lack of shallow convection during the development of organized convection. This feature is due to the reduced number of cloud types that makes the convection scheme unable to consider coexistence of shallow and deep convection at the same time. Eventually, this type of convection scheme tends to simulate drier condition after Day 0 neglecting the moisture supply from detrainment of shallow convection, leading to shorter lifetime of the MJO. AMIP-SCC that used the identical convective closure as the TK scheme failed to simulate sufficient cloud mass flux especially in the low level and resulted in weaker organized convection. The failure is due to the fact that this convective closure, which does not employ density-weighted CAPE, tends to underestimate the cloud mass flux of the convective clouds, since the CAPE change is not readily connected with mass flux change. Further mechanism for this underestimation remains an open question. Based on these results, it can be concluded that the entrainment parameterization is necessary, and the spectral representation and the convective closure employed in the SC scheme contribute for better MJO simulation.

6. Summary and Conclusion

A spectral cumulus parameterization (SC scheme) was implemented in the ICON-A as an alternative to the Tiedtke-Nordeng scheme (TK scheme). Compared to its original formulation, the SC scheme was modified by a differentiation in the convective closure and turbulent entrainment (detrainment). All other processes of the ICON-A, and in particular the tuning parameters, remained unchanged. The effect of the exchanged convection scheme was evaluated by a comparison of two AMIP experiments, AMIP-SC and AMIP-TK, against the observational and reanalysis data.

A standardized error analysis for the simulated climatology was first conducted to compare the errors of both experiments. AMIP-SC indicated comparable climatological errors in tropics and southern extratropics and

slightly improved northern extratropics compared to AMIP-TK. In the analysis for each variable, the errors of the meridional wind were remarkably improved regardless of latitudes. The mean states of the simulated climate were evaluated against the observation. AMIP-SC improved precipitation biases and radiative flux biases, especially in the western Pacific. Even though AMIP-SC showed increased biases of precipitation over land and different radiative biases over ocean, their magnitudes were not significant. Biases of cloud cover were common for AMIP-TK and AMIP-SC as cloud cover was underestimated in subtropical regions, and the cloud cover slightly more underestimated in AMIP-SC. Insufficient cloud cover over the Southern Ocean was common for both cases and it seemed to need further improvements in the physics.

Tropical variability was analyzed in terms of interannual and intraseasonal time scales. The atmospheric response to ENSO was examined using monthly precipitation. Both cases showed clear precipitation responses to the SST anomalies, but their patterns were different. As indicated in the comparison of the mean state, in the western Pacific, AMIP-SC reproduced the negative response to the SST anomaly, while AMIP-TK did not. The comparison of power spectra of CCEWs in wavenumber-frequency diagrams indicated that the SC scheme could not improve the too weak power spectra in the symmetric component that appeared in AMIP-TK. However, AMIP-SC reproduced the MJO signals. From the lag-longitude and lag-latitude correlation diagrams for OLR and zonal wind anomalies, AMIP-SC successfully simulated MJO features. The combined EOF analysis revealed that the variances simulated by AMIP-TK were not explained well by EOF1 and EOF2. On the other hand, the variances simulated by AMIP-SC were explained qualitatively well, but the explained variances were somewhat smaller than observed. It was apparent that the life cycle composite of MJO generated by AMIP-SC showed realistic trends and strength compared to the observations.

Additional sensitivity experiments were performed to reveal which parameterization in the convection schemes affected the reproducibility of MJO. Two modified SC schemes were considered: the SCS scheme (number of cloud types was reduced to one) and the SCC scheme (identical convective closure of TK scheme was adopted), and their experiments were referred to as AMIP-SCS and AMIP-SCC, respectively. Both cases simulated weaker signals of equatorial Kelvin, mixed-Rossby gravity waves and MJO than AMIP-SC, even though the cases partly reproduced lag-longitude correlations as simulated by AMIP-SC. In addition, percentages of variances explained by EOFs became smaller than those of AMIP-SC. A quantitative analysis conducted for evaluating MJO fidelity of all cases indicated that the fidelity was better in the order of AMIP-SC, AMIP-SCS, AMIP-SCC, and AMIP-TK.

Analysis on composited fields with respect to the organized convection was conducted to understand the differences in the structure of simulated organized convection. The composited fields revealed that time mean atmospheric conditions during organized convection occurred were different depending on the convection schemes. The time mean condition of AMIP-TK in the low level was much warmer and drier than other cases and was found to be more significant than the anomalous fields. This suggests that shallow convection was dominant and it suppressed further convection in this case. Composited convective heating and entrainment originating from deep and shallow convection were analyzed. The results indicated that AMIP-TK simulated weaker heating by excessive entrainment of shallow convection. AMIP-TK also showed entrainment profiles for deep and shallow convection were separated in the altitude. In the sensitivity cases, replaced parameterization changed heating and entrainment profiles, as AMIP-SCS (AMIP-SCC) showed reduced heating and entrainment for shallow (deep) convection. By these features, it was assumed that AMIP-SCS lacked moisture supply from shallow clouds, and AMIP-SCC simulated weaker deep convection. This investigation also indicated that the entrainment parameterization of the SC scheme appeared to have entrainment profiles, which are continuous in altitude in contrast to the TK scheme.

Finally, the moisture variation in the MJO life cycle was investigated to clarify which differences between the convection schemes influenced the organized structure of the MJO. The composited specific humidity anomalies indicated that AMIP-TK and AMIP-SCC simulated weaker organized humidity anomalies, and AMIP-SCS simulated larger negative anomaly after the organized structure, whereas AMIP-SC succeeded in simulating the feature well. The different features of humidity amplification were analyzed from tendencies of humidity. The vertical advection and physics tendencies were found to be dominant, aligning with the results of preceding study. Further analysis on the anomalous tendencies of humidity revealed that tendencies by longwave radiation and detrainment from the low-level clouds were found to cause dominant

differences between the cases. In AMIP-TK, longwave heating caused the largest difference in the humidity amplification; that is, longwave heating did not appear well in this case, since warmer and drier condition disturbed cloud condensate to form from the low to upper levels, and much longwave cooling that resulted in strong drying occurred. In AMIP-SCS and AMIP-SCC, lack of detrainment from the low-level clouds caused the largest difference. When the organized convection occurred, these cases simulated less low-level convection (shallow or lower part of deep convection), and thus, lacked moisture supply by detrainment, leading to failure in sustaining the humidity amplification sufficiently.

In conclusion, the SC scheme is capable of simulating tropical variability better than the original scheme of ICON-A model. The SC scheme improved especially the intraseasonal variability, while the climatological errors remained comparable. These results support the validity of this scheme in different AGCMs. Using the sensitivity experiments, we found the superiority of the SC scheme to the TK scheme was obtained not only by the entrainment parameterization but also by spectral representation of clouds and the convective closure. This result means that the performance of in-cloud (entrainment) parameterization of the SC scheme, which is a key parameterization of this convection scheme that can realize continuous entrainment between different cloud types, is supported by both the spectral representation and the convective closure. Without these parameterizations, the performance will be degraded. The spectral representation and convective closure contributed to reproduce the moisture supply from the shallow convection to sustain the organized convection and simulating reasonable cloud mass flux.

Because the inferior reproducibility of the MJO by the TK scheme originates from dominant shallow convection with excessive entrainment and discontinuous entrainment profiles among the cloud types, at least this feature should be corrected. Possible solutions for this problem are reducing the strong entrainment rate employed in shallow convection and introduce continuous entrainment parameterization for different cloud types. In addition, changing the convective closure from the present to the density-weighted CAPE type closure may be the another possible solution. The present analysis also revealed that some biases, and their solutions still remained as an open question. For further improvement, improving other physical parameterizations, such as a large-scale cloud scheme (Sundqvist et al., 1989) or a planetary boundary layer scheme (Pithan et al., 2015) might be effective because these schemes parameterize unresolved moisture variations in the troposphere. The atmosphere-ocean coupling that is lacking in the AMIP simulation here also might affect the reproducibility of the tropical variability (e.g., Crueger et al., 2013). Thus, a further evaluation using a coupled model should be performed in a future study.

Appendix A: Turbulent Entrainment and Detrainment

A.1. Formulations

In the implementation of the SC scheme in ICON-A, turbulent updraft entrainment and detrainment were introduced. This is because, in the preliminary experiment, the convection scheme with the set of physical parameterizations of ICON-A was found to produce too much cloud cover in the tropics, and it was necessary to enhance the dilution of convection through turbulent mixing as a tuning for the better atmospheric energy budget. Assuming equations (7) and (8) provide the dominant components, the turbulent entrainment and detrainment rates based on (ECMWF, 2008; 2014) are given as

$$\epsilon_u^{trb} = \epsilon_0 f_e (1.3 - RH) f_{scale}, \quad f_{scale} = \left[\frac{q_{sat}(\bar{p}, \bar{T})}{q_{sat}(\bar{p}, \bar{T})_{base}} \right]^3, \quad (A1)$$

$$\delta_u^{trb} = \begin{cases} \epsilon_u^{trb} (1.6 - RH), & \text{for shallow convection} \\ \delta_0 (1.6 - RH), & \text{for deep shallow convection} \end{cases} \quad (A2)$$

where $\epsilon_0 = 1 \times 10^{-3} \text{ m}^{-1}$, $f_e = 0.5$ for deep convection, $f_e = 3$ for shallow convection, and $\delta_0 = 0.75 \times 10^{-4} \text{ m}^{-1}$. Then, f_{scale} is the scaling factor that considers height dependence of the entrainment rate (Bechtold et al., 2008), q_{sat} the saturation specific humidity as a function of environmental temperature and pressure, and RH the relative humidity of the environment. Since the convective depth is unknown before the budget equations of heat and moisture are vertically integrated, a provisional calculation is performed using parameters for deep convection and different parameters are then applied to each convection depending on the estimated convective depth. The threshold convective depth to identify deep convection is defined to be 180 hPa based on Bechtold et al. (2014), and otherwise, they are identified as shallow convection.

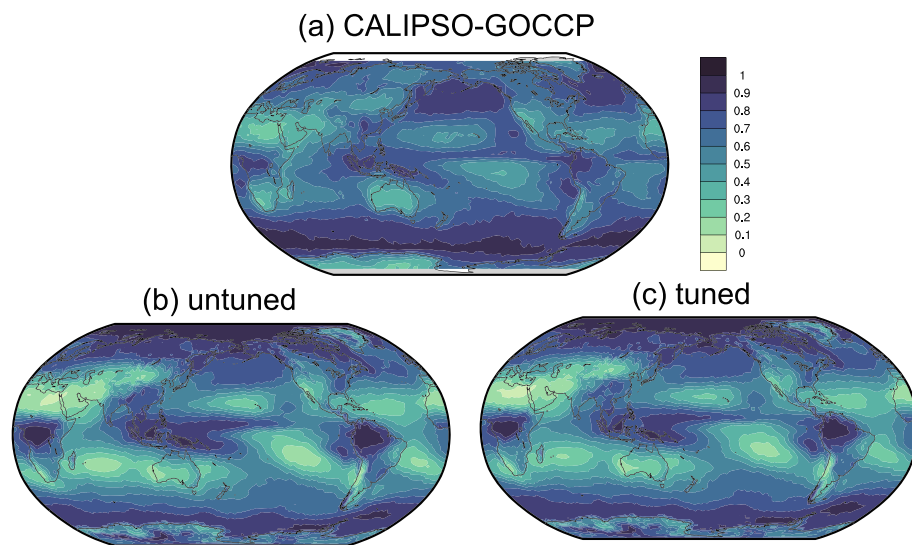


Figure A1. (a–c) Comparison of annual mean total cloud cover for untuned and tuned cases. CALIPSO-GOCCP data used as the reference were averaged over 10 years from 2007.

A.2. Evaluation

Annual mean cloud cover distributions of untuned and tuned experiments are compared in Figure A1. The cloud cover of untuned case apparently shows that the amount in tropics (subtropics) is larger (smaller) than those of the observation. The biases of cloud cover are mitigated in the tuned case as the amount in tropics (subtropics) became smaller (larger) than those of untuned case. Standardized errors of cloud cover and radiative fluxes were estimated using the results of untuned case as a reference (Figure A2). As intended in the tuning for the cloud cover, the errors are mostly reduced over the whole regions. Improvements in the radiative fluxes are mainly obtained from OLR, while the errors of OSR show comparable values to those of tuned case. Resulting differences of global energy budgets from the observation are approximately -1 W/m^2 for the untuned case and -2 W/m^2 for the tuned case; thus, the budget of tuned case became slightly worse than the that of untuned case. However, the tuned case improved mean state of cloud cover and radiative fluxes; therefore, we used the tuned case since the better mean state is considered more important for the model's climatology.

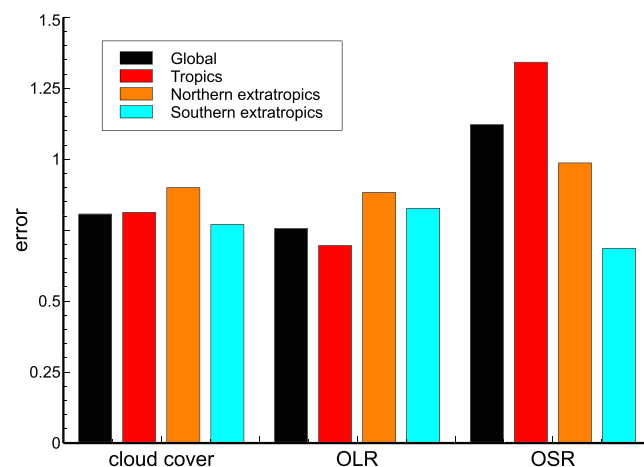


Figure A2. Standardized errors of the cloud cover, OLR and OSR for the tuned case with respect to the untuned case. A value less than 1 means improvement of the tuned case compared to the untuned case.

Table B1

Ratios of Eastward/Westward Propagation R for OLR, U_{850} , U_{200} , and Precipitation (R_{OLR} , $R_{U_{850}}$, $R_{U_{200}}$, and R_{PR}), and Mean of These Values as R_{mean}

Case	Ratios of eastward/westward propagation R					Fractional explained variance F			
	R_{OLR}	$R_{U_{850}}$	$R_{U_{200}}$	R_{PR}	R_{mean}	F_{OLR}	$F_{U_{850}}$	$F_{U_{200}}$	MJO_{sc}
Observation	3.13	3.24	2.46	2.80	2.91	43.8	56.8	29.0	0.914
AMIP-TK	1.13	1.03	1.46	1.04	1.16	39.2	25.7	9.0	0.251
AMIP-SC	1.83	2.18	1.64	1.83	1.87	36.7	46.8	16.1	0.564
AMIP-SCS	1.73	1.87	1.73	1.49	1.70	36.2	43.3	13.5	0.504
AMIP-SCC	1.58	2.04	1.70	1.61	1.73	32.5	46.5	12.5	0.487

Note. Sums of fractional explained variances (F_{OLR} , $F_{U_{850}}$, and $F_{U_{200}}$) of the two first leading modes of the multivariate EOF are also shown. See text for details of the MJO score MJO_{sc} . For observation, AVHRR, NCEP/NCAR reanalysis, and pentad CMAP data (Xie & Arkin, 1997) (1979–1988) were used to calculate each variable.

Appendix B: MJO Score

The fidelity of MJO simulated by each case was evaluated using a quantitative analysis using MJO metric which was proposed by Crueger et al. (2013). The MJO metric uses mean ratio of eastward/westward propagation R_{mean} to evaluate eastward propagating features of MJO signals and uses values of multivariate EOF for OLR F_{OLR} to evaluate MJO strength. The values of each R_{mean} and F_{OLR} and related values can be obtained from the U.S. CLIVAR MJO diagnostics (Waliser et al., 2009) and the methods described in Crueger et al. (2013). The MJO score MJO_{sc} is calculated by following equation:

$$MJO_{sc} = \sqrt{[\max(1, R_{mean}) - 1] \cdot F_{OLR}/100}, \quad (B1)$$

which means that the case showing R_{mean} less than 1 fails to reproduce MJO. The values of R_{mean} and F_{OLR} including related values and resulting MJO_{sc} are summarized in Table B1. As expected from the qualitative analysis, AMIP-TK and AMIP-SC show the worst and the best MJO scores, respectively. Among the cases using SC and SC-derived schemes, the scores are better (closer to the observation) in the order of AMIP-SC, AMIP-SCS, and AMIP-SCC.

Appendix C: Differences in Nonanomalous Moistening Terms of Moisture Budget Equation

C.1. All Terms

Since AMIP-SC showed the best results regarding the MJO, understanding the differences of the tendencies simulated in the other cases may be a key to identify the causes of inferior results. Figure C1 compares differences of composited tendencies of each term of equation (13) from those of AMIP-SC. The comparison indicates that AMIP-TK simulated much smaller moistening tendencies for the first and second terms, and the decrease is significant in the second term below the 600-mb level. On the other hand, AMIP-SCS and AMIP-SCC simulated smaller moistening tendency in the lower levels, and the negative differences in the moistening are mainly caused by the third term.

C.2. Second Term

The significance of each process included in the second term of equation (13) is compared in Figure C2. The smaller moistening in AMIP-TK is found to be caused by the longwave radiation, as the value indicates greater negative value in the low and middle levels. Even though relative moistening due to liquid-ice transition is significant in AMIP-TK, the moistening effect is narrow in the levels, and negative difference in the tendencies by longwave radiation is dominant. Since the shortwave impact is significant in the lower levels at the same time, radiative cooling and heating are considered to occur more in lower levels compared to the other cases. In the profiles of AMIP-SCS and AMIP-SCC, differences of moistening or drying effects derived from the second term are relatively small, but the tendency by longwave radiation in AMIP-SCS contributed to less moistening below 400-mb level.

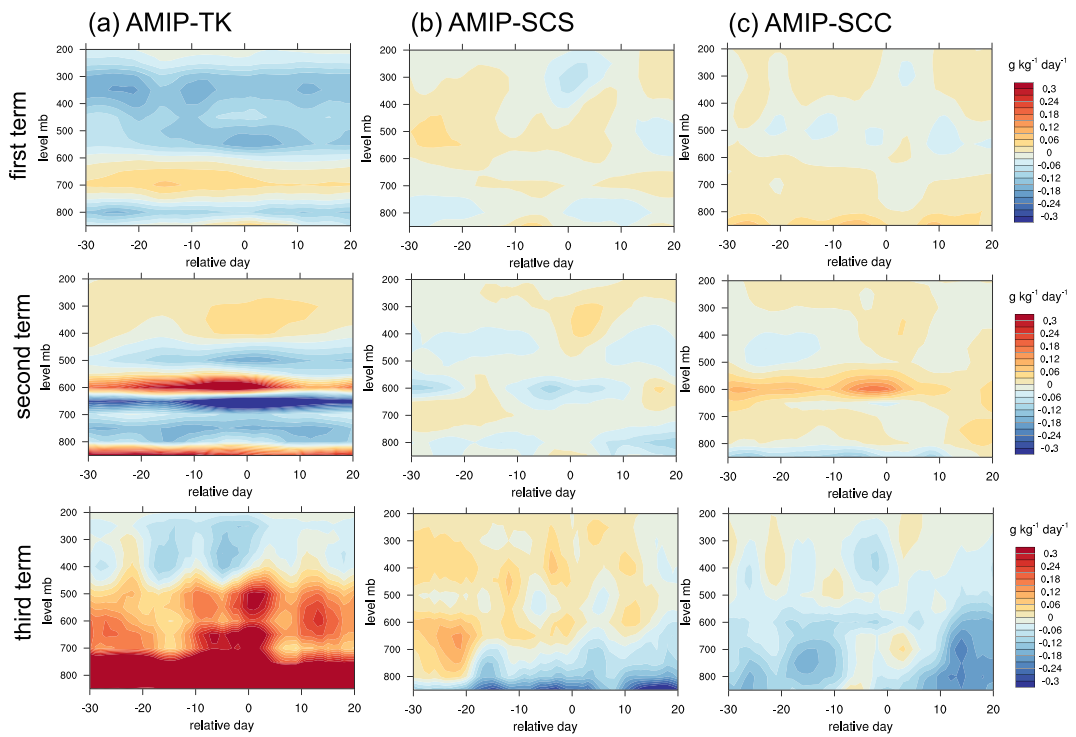


Figure C1. As Figure 18 but for differences of composited nonanomalous tendencies of each term in equation (13) from those of AMIP-SC.

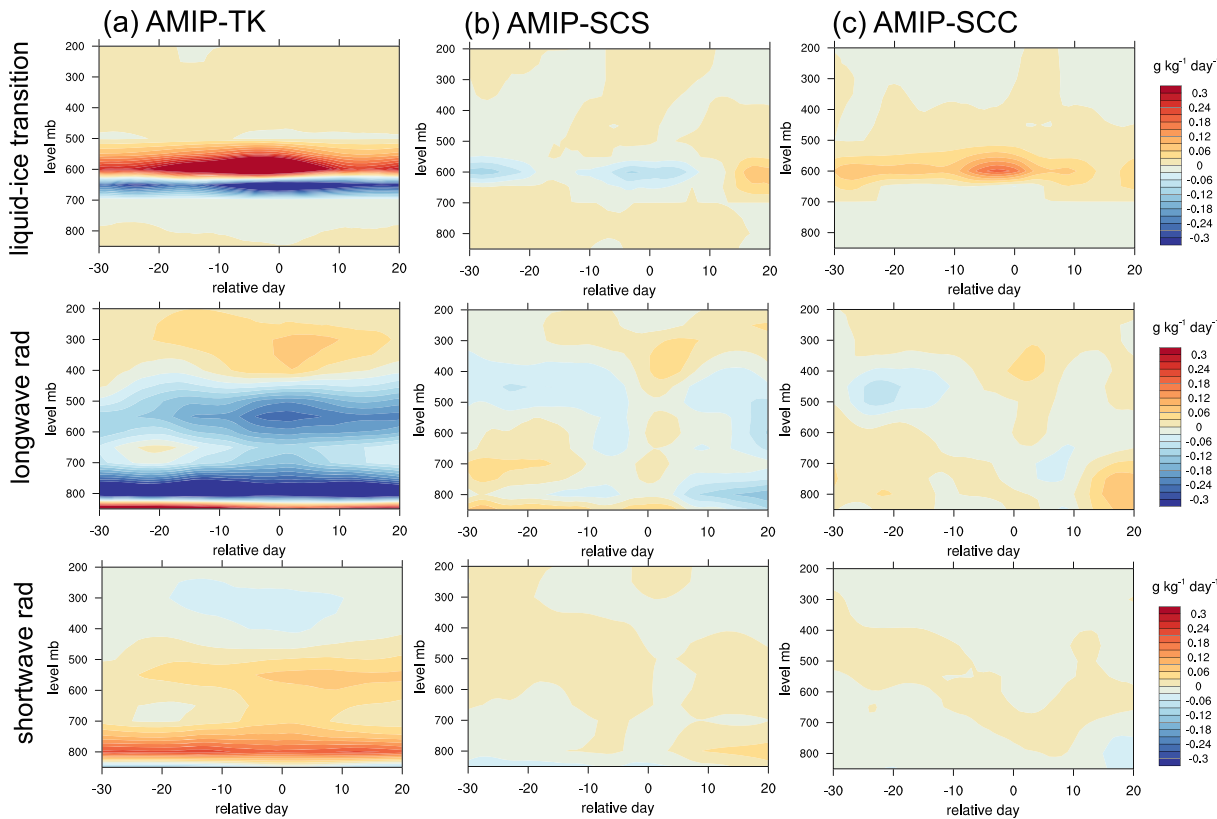


Figure C2. As Figure 18 but for differences of composited nonanomalous tendencies included in the second term of equation (13) from those of AMIP-SC. Each panel indicate tendencies by (top) liquid-ice transition, (middle) longwave radiation, and (bottom) shortwave radiation. Tendencies by diffusion are excluded since their significance appear only near the surface.

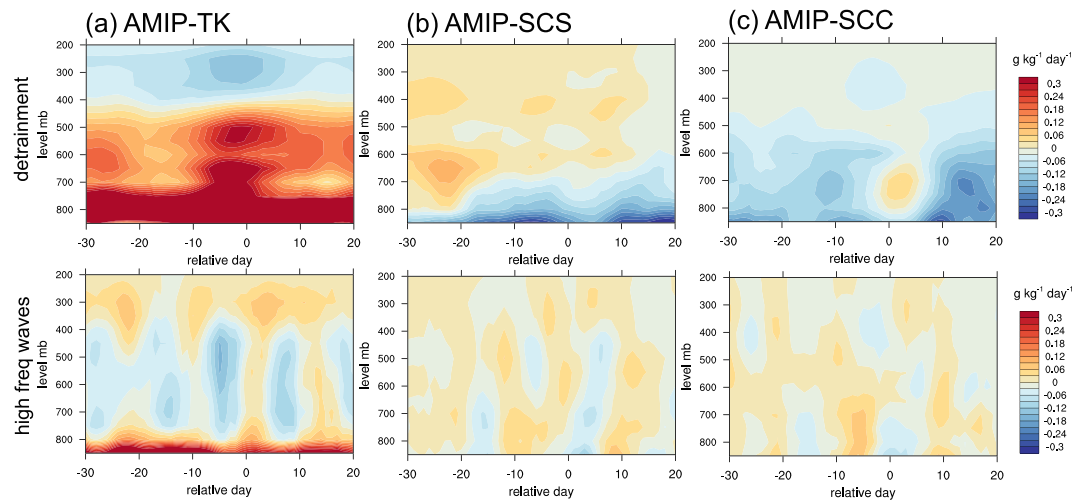


Figure C3. As Figure 18 but for differences of compositing nonanomalous tendencies included in the third term of equation (13) from those of AMIP-SC. Each panel indicates tendencies by (top) detrainment, and (bottom) high frequency waves.

C.3. Third Term

Significances of terms in the third term of equation (13) are compared in Figure C3. Moistening tendency by detrainment in AMIP-TK is more significant than in other cases below 400 mb, and the moistening is less above 400 mb. This result suggests that weaker convection, which has lower cloud top and larger detrainment (e.g., Gregory, 2001; Romps, 2010; Tiedtke, 1989) in the low to middle level is more dominant in this case. The difference in the moistening or drying of high-frequency waves is also large, and a greater negative difference appears around Day 0. In both AMIP-SCS and AMIP-SCC, the difference in the moistening by the detrainment from low-level clouds is significant, and the contribution to the negative difference in the column process is prominent. Differences in the high-frequency waves appear to be positive or negative but insignificant at almost all levels.

References

- Adler, R. F., Huffman, G. J., Chang, A., Ferraro, R., Xie, P., Janowiak, J., et al. (2003). The version 2 Global Precipitation Climatology Project (GPCP) monthly precipitation analysis (1979–present). *Journal of Hydrometeorology*, 4, 1147–1167.
- Arnold, N. P., & Randall, D. A. (2015). Global-scale convective aggregation: Implication for the Madden-Julian oscillation. *Journal of Advances in Modeling Earth Systems*, 7, 1499–1518. <https://doi.org/10.1002/2015MS000498>
- Baba, Y. (2019). Spectral cumulus parameterization based on cloud-resolving model. *Climate Dynamics*, 52, 309–334.
- Bechtold, P., Köhler, M., Jung, T., Francisco, D.-R., Leutbecher, M., Rodwell, M. J., et al. (2008). Advances in simulating atmospheric variability with the ECMWF model: From synoptic to decadal time-scales. *Quarterly Journal of the Royal Meteorological Society*, 134, 1337–1351.
- Bechtold, P., Semane, N., Lopez, P., Chaboureau, J.-P., Beljaars, A., & Bormann, N. (2014). Representing equilibrium and nonequilibrium convection in large-scale models. *Journal of the Atmospheric Sciences*, 71, 734–753.
- Bellucci, A., Gualdi, S., & Navarra, A. (2010). Double-ITCZ syndrome in coupled general circulation models: The role of large-scale vertical circulation regimes. *Journal Climate*, 23, 1127–1145.
- Bodas-Salcedo, A., Williams, K. D., Ringer, M. A., Beau, I., Cole, J. N. S., Dufresne, J.-L., et al. (2014). Origins of the solar radiation biases over the Southern Ocean in CMIP2 models. *Journal Climate*, 27, 41–56.
- Cai, G., Zhang, G. J., & Zhou, T. (2013). Impacts of shallow convection on MJO simulation: A moist static energy and moisture budget analysis. *Journal Climate*, 26, 2417–2431.
- Chefher, H., Bony, S., Winker, D. M., Cesana, G., Dufresne, J.-L., Minnis, P., et al. (2010). The GCM oriented CALIPSO cloud product (CALIPSO-GOCCP). *Journal of Geophysical Research*, 115, D00H16. <https://doi.org/10.1029/2009JD012251>
- Chikira, M. (2014). Eastward-propagating intraseasonal oscillation represented by Chikira-Sugiyama cumulus parameterization. Part II: Understanding moisture variation under weak temperature gradient balance. *Journal of the Atmospheric Sciences*, 71, 615–639.
- Chikira, M., & Sugiyama, M. (2010). A cumulus parameterization with state dependent entrainment rate. Part I: Description and sensitivity to temperature and humidity profiles. *Journal of the Atmospheric Sciences*, 67, 2171–2193.
- Chikira, M., & Sugiyama, M. (2013). Eastward-propagating intraseasonal oscillation represented by Chikira-Sugiyama cumulus parameterization. Part I: Comparison with observation and reanalysis. *Journal of the Atmospheric Sciences*, 70, 3920–3939.
- Crueger, T., Giorgetta, M. A., Brokopf, R., Esch, M., Fiedler, S., Hohenegger, C., et al. (2018). ICON-A, the atmosphere component of the ICON earth system model. Part II: Model evaluation. *Journal of Advances in Modeling Earth Systems*, 10, 1613–1637. <https://doi.org/10.1029/2017MS001242>
- Crueger, T., Stevens, B., & Brokoff, R. (2013). The Madden-Julian oscillation in ECHAM6 and the introduction of an objective MJO metric. *Journal Climate*, 26, 3241–3257.

Acknowledgments

A part of this work was done during Yuya Baba's visit at the Max Planck Institute for Meteorology (MPI-M). Y. B. thanks Monika Esch of MPI-M for her technical support and Traute Crueger of MPI-M for her comments on the analysis. Computations were performed on the Mistral supercomputer of Deutsches Klimarechenzentrum (DKRZ). Most of the figures were drawn using the NCAR Command Language (Version 6.4.0) [Software]. (2017). Boulder, Colorado: UCAR/NCAR/CISL/TDD (<https://doi.org/10.5065/D6WD3XH5>). The code of ICON-A is available under the ICON Software License Agreement (ISLA) Version 2.1 of the German Weather Service DWD and the MPI-M (<https://www.mpgmet.mpg.de/en/science/models/license>). Primary data and scripts used in this study are stored in the DKRZ long-term archive and available from WDCC Data Portal CERA (<https://cera-www.dkrz.de/WDCC/ui/cerasearch/>) entry? acronym=DKRZ_LTA_287_ds00002). The reanalysis data used in the present study are available, as ERA-interim (ECMWF, <http://apps.ecmwf.int/datasets/data>), GPCP, ICOADS, NCEP/NCAR reanalysis and CMAP (NOAA ESRL PSD, <https://www.esrl.noaa.gov/psd/data/gridded>), CERES-EBAF (NASA Langley Research Center, <http://ceres.larc.nasa.gov/>), and CALIPSO-GOCCP (CFMIP-Obs website, <https://climserv.ipsl.polytechnique.fr/cfmip-obs/> Calipso_goccp.html).

- Dee, D. P., Uppala, S. M., Simmons, A. J., Berrisford, P., Poli, P., Kobayashi, S., et al. (2011). The ERA-interim reanalysis: Configuration and performance of the data assimilation system. *Quarterly Journal of the Royal Meteorological Society*, 137, 553–597.
- Del Genio, A. D., & Chen, Y. (2015). Cloud-radiative driving of the Madden-Julian oscillation as seen by the A-Train. *Geophysical Research Letters*, 120, 5344–5356. <https://doi.org/10.1002/2015JD023278>
- Derbyshire, S. H., Maidens, A. V., Milton, S. F., Stratton, R. A., & Willett, M. R. (2011). Adaptive detrainment in a convective parameterization. *Quarterly Journal of the Royal Meteorological Society*, 137, 1856–1871.
- ECMWF (2008). Part IV: Physical processes. IFS documentation CY33R1, <http://www.ecmwf.int/en/forecasts/documentation-and-support/changes-ecmwf-model/ifs-documentation>, accessed 15 Mar 2018
- ECMWF (2014). Part IV: Physical processes. IFS documentation CY41R1, <http://www.ecmwf.int/en/forecasts/documentation-and-support/changes-ecmwf-model/ifs-documentation>, accessed 17 Feb 2016
- Eyring, V., Bony, S., Meehl, G. A., Senior, C. A., Stevens, B., Stouffer, R. J., & Taylor, K. E. (2016). Overview of the Coupled Model Intercomparison Project phase 6 (CMIP6) experimental design and organization. *Geoscientific Model Development*, 9, 1937–1958.
- Fiedler, S., Stevens, B., & Mauritsen, T. (2017). On the sensitivity of anthropogenic aerosol forcing to model-internal variability and parameterizing a Twomey effect. *Journal of Advances in Modeling Earth Systems*, 9, 1325–1341. <https://doi.org/10.1002/2017MS000932>
- Giorgetta, M. A., Brokopf, R., Crueger, T., Esch, M., Fiedler, S., Helmert, J., et al. (2018). ICON-A, the atmospheric component of the ICON Earth system model. Part I: Model description. *Journal of Advances in Modeling Earth Systems*, 10, 1613–1637. <https://doi.org/10.1029/2017MS001242>
- Giorgetta, M. A., Jungclaus, J., Reick, C. H., Legutke, S., Bader, J., Böttinger, M., & Stevens, B. (2013). Climate and carbon cycle changes from 1850 to 2100 in MPI-ESM simulations for coupled model intercomparison project phase 5. *Journal of Advances in Modeling Earth Systems*, 5, 572–597.
- Giorgetta, M. A., Roeckner, E., Maurisen, T., Bader, J., Crueger, T., Esch, M., et al. (2013). The atmospheric general circulation model ECHAM6: Model description. *Reports on Earth System Science*, 135.
- Gregory, D. (2001). Estimation of entrainment rate in simple models of convective clouds. *Quarterly Journal of the Royal Meteorological Society*, 127, 53–72.
- Hirons, L. C., Innes, P., Vitart, F., & Bechtold, P. (2013). Understanding advances in the simulation of intraseasonal variability in the ECMWF model. Part I: The representation of MJO. *Quarterly Journal of the Royal Meteorological Society*, 139, 1417–1426.
- Huffman, G. J., Adler, R. F., Morrissey, M., Bolvin, D. T., Curtis, S., Joyce, R., et al. (2001). Global precipitation at one-degree daily resolution from multi-satellite observations. *Journal of Hydrometeorology*, 2, 36–50.
- Hung, M.-P., Lin, J.-L., Wang, W., Kim, D., Shinoda, T., & Weaver, S. J. (2013). MJO and convectively coupled equatorial waves simulated by CMIP5 climate models. *Journal Climate*, 26, 6185–6214.
- Kalnay, E., Kanamitsu, M., Kistler, R., Collins, W., Deaven, D., Gandin, L., et al. (1996). The NCEP/NCAR 40-year reanalysis project. *Bulletin of the American Meteorological Society*, 77, 437–471.
- Kim, D., Sperber, K., Stern, W., Waliser, D., Kang, I.-S., Maloney, E., et al. (2009). Application of MJO simulation diagnostics to climate model. *Journal Climate*, 22, 6413–6436.
- Liebmann, B., & Smith, C. A. (1996). Description of a complete (interpolated) outgoing longwave radiation dataset. *Bulletin of the American Meteorological Society*, 77, 1275–1277.
- Lin, J.-L., Lee, M.-I., Kim, D., Kang, I.-S., & Frierson, D. M. W. (2008). The impact of convective parameterization and moisture triggering on AGCM-simulated convectively coupled equatorial waves. *Journal of Climate*, 21, 883–909.
- Loeb, N. G., Wielicki, B. A., Doelling, D. R., Smith, G. L., Keyes, D. F., Kato, S., et al. (2009). Toward optimal closure of the Earth's top-of-atmosphere radiation budget. *Journal Climate*, 22, 748–766.
- Madden, R. A., & Julian, P. R. (1971). Detection of a 40–50 day oscillation in the zonal wind in the tropical Pacific. *Journal of the Atmospheric Sciences*, 28, 702–708.
- Meinshausen, M., Vogel, E., Nauels, A., Lorbacher, K., Meinshausen, N., Etheridge, D. M., & Weiss, R. (2017). Historical greenhouse gas concentrations for climate modelling (CMIP6). *Geoscientific Model Development*, 10, 2057–2116.
- Möbis, B., & Stevens, B. (2012). Factors controlling the position of the intertropical convergence zone on an aquaplanet. *Journal of Advances in Modeling Earth Systems*, 4, M00A04.
- Neale, R. B., Richter, J. H., & Jochum, M. (2008). The impact of convection on ENSO: From a delayed oscillator to a series of events. *Journal Climate*, 21, 5904–5924.
- Nordeng, T. E. (1994). Extended versions of the convective parameterization scheme at ECMWF and their impact on the mean and transient activity of the model in the tropics. *ECMWF Technical Memorandum*, 206, 41.
- North, G. R., Bell, T. L., & Cahalan, R. F. (1982). Sampling errors in the estimation of empirical orthogonal functions. *Monthly Weather Review*, 110, 699–706.
- PCMDI (2017). input4MIPs: Boundary condition and forcing datasets for CMIP6. <https://esgf-node.llnl.gov/projects/input4mips/>, accessed 10 Oct 2017.
- Pithan, F., Angevine, W., & Mauritsen, T. (2015). Improving a global model from boundary layer: Total turbulent energy and the neutral limit Prandtl number. *Journal of Advances in Modeling Earth Systems*, 7, 791–805. <https://doi.org/10.1002/2014MS000382>
- Reichler, T., & Kim, J. (2008). How well do coupled models simulate today's climate? *Bulletin of the American Meteorological Society*, 89(3), 303–311.
- Romps, D. M. (2010). A direct measure of entrainment. *Journal of the Atmospheric Sciences*, 67, 1908–1927.
- Simpson, J., & Wiggert, V. (1969). Models of precipitating cumulus towers. *Monthly Weather Review*, 97, 471–489.
- Sobel, A., Nilsson, J., & Polvani, L. M. (2001). The weak temperature gradient approximation and balanced tropical moisture waves. *Journal of the Atmospheric Sciences*, 58, 3650–3665.
- Stevens, B., Fiedler, S., Kinne, S., Peters, K., Rast, S., Müsse, J., & Smith, S. J. (2017). MACv2-SP: A parameterization of anthropogenic aerosol optical properties and an associated Twomey effect for use in CMIP6. *Geoscientific Model Development*, 10, 433–452.
- Stevens, B., Giorgetta, M. A., Esch, M., Mauritsen, M., Crueger, T., Rast, S., & Roeckner, E. (2013). Atmospheric component of the MPI-M Earth system model: ECHAM6. *Journal of Advances in Modeling Earth Systems*, 5, 146–172. <https://doi.org/10.1002/jame.20015>
- Sundqvist, H., Berge, E., & Kristjansson, E. (1989). Condensation and cloud parameterization studies with a mesoscale numerical weather prediction model. *Monthly Weather Review*, 117, 1641–1657.
- Taylor, K., Williamson, D., & Zwiers, F. (2000). The sea surface temperature and sea-ice concentration boundary conditions for AMIP II simulations. *PCMDI Report*, 60(28).
- Tiedtke, M. (1989). A comprehensive mass flux scheme for cumulus parameterization in large-scale models. *Monthly Weather Review*, 117, 1779–1800.

- Waliser, D., Sperber, K., Hendon, H., Kim, D., Maloney, E., Wheeler, M., et al. (2009). MJO simulation diagnostics. *Journal Climate*, 22, 3006–3030.
- Wan, H., Giorgetta, M. A., Zängl, G., Restelli, M., Majewski, D., Bonaventura, L., et al. (2013). The ICON-1.2 hydrostatic atmospheric dynamical core on triangular grids—Part 1: Formulation and performance of the baseline version. *Geoscientific Model Development*, 6, 735–763.
- Watanabe, M., Chikira, M., Imada, Y., & Kimoto, M. (2011). Convective control of ENSO simulated in MIROC. *Journal Climate*, 24, 543–562.
- Wheeler, M., & Hendon, H. H. (2004). An all-season real-time multivariate MJO index: Development of an index for monitoring and prediction. *Journal of the Atmospheric Sciences*, 132, 1917–1932.
- Woodruff, S. D., Worley, S. J., Lubker, S. J., Ji, Z., Freeman, J. E., Berry, D. I., et al. (2011). ICOADS Release 2.5: Extensions and enhancements to the surface marine meteorological archive. *International Journal of Climatology*, 31, 951–967.
- Wu, X., Liang, X.-Z., & Zhang, G. J. (2003). Seasonal migration of ITCZ precipitation across the equator: Why can't GCMs simulate it? *Geophysical Research Letters*, 30, 1824. <https://doi.org/10.1029/2003GRL017198>
- Xie, P., & Arkin, P. A. (1997). Global precipitation: A 17-year monthly analysis based on gauge observations, satellite estimates, and numerical model outputs. *Bulletin of the American Meteorological Society*, 78, 2539–2558.
- Zängl, G., Reinert, D., Ripodas, P., & Baldauf, M. (2015). The ICON (ICOrahedral Non-hydrostatic) modelling framework of DWD and MPI-M: Description of the non-hydrostatic dynamical core. *Quarterly Journal of the Royal Meteorological Society*, 141, 563–579.
- Zhang, C. (2005). Madden-Julian oscillation. *Reviews of Geophysics*, 43, RG2003. <https://doi.org/10.1029/2004RG000158>
- Zhang, G. J., & Song, X. (2009). Interaction of deep and shallow convection is key to Madden-Julian oscillation simulation. *Geophysical Research Letters*, 36, L09708. <https://doi.org/10.1029/2009GL037340>